Nuclear Instruments and Methods in Physics Research A289 (1990) 115–138
North-Holland

TEST OF THE ZEUS FORWARD CALORIMETER PROTOTYPE

The ZEUS Calorimeter Group
U. BEHRENS [1], J. CRITTENDEN [2], K. DIERKS [3], G. DREWS [4], J. ENGELEN [5], B. FRISKEN [6], R. HAMATSU [7], D. HANNA [8], U. HOLM [1], M.A. GARCIA [9], D. HASELL [6], T. HASEGAWA [10], R. KLANNER [4], O. KÖLL [3], P. KOOIJMAN [5], U. KÖTZ [4], M. KRÄMER [2], J. KRÜGER [3], J. LEHMANN [11], G. LEVMAN [12], D. LÜKE [4], J. MARTIN [12], P. NEELIN [8], M. ROHDE [4], E. ROS [4], F. SELONKE [4], G. SMITH [13], G. STAIRS [12], J. STRAVER [5], H. TIECKE [5], J.F. TROCÓNIZ [9], T. TSURUGAI [3], W. VOGEL [1], K. WICK [1], M. WÜLKER [11] and C. YOUNGMAN [3]

[1] *University of Hamburg, I. Institut, FRG* *
[2] *University of Bonn, FRG* *
[3] *University of Hamburg, II. Institut, FRG* *
[4] *DESY, Hamburg, FRG*
[5] *NIKHEF-H, Amsterdam, The Netherlands*
[6] *York University, North York, Ont., Canada* **
[7] *Tokyo Metropolitan University, Japan*
[8] *McGill University, Montreal, Que., Canada* **
[9] *Universidad Autónoma de Madrid, Spain* +
[10] *INS, University of Tokyo, Japan*
[11] *University of Freiburg, FRG* *
[12] *University of Toronto, Canada* **
[13] *University of Manitoba, Winnipeg, Man., Canada* **

Received 20 October 1989

Four prototype modules following the same design as the ZEUS forward calorimeter (FCAL) modules have been constructed and tested with electrons, hadrons and muons in the momentum range of 1 to 100 GeV/c. The main topics under investigation were: calibration, uniformity of response, noise, light yield, energy resolution and the electron to hadron response (e/h ratio). The result of the measurements is presented and the expected performance of the FCAL is discussed in the light of these results.

1. Introduction

The ZEUS Collaboration [1] has proposed a uranium–scintillator sandwich calorimeter as the key to study the physics of high energy electron–proton interactions at the HERA collider. In order to achieve these physics goals the calorimeter should satisfy the following requirements:

- hermeticity,
- equal response for electrons and hadrons (e/h = 1),
- jet energy resolution of $\sigma(E)/E = 35\%/\sqrt{E} \oplus 2\%$, where E is the energy of the jet and $\oplus$ indicates a quadratic sum,
- angular resolution for jets better than 10 mrad and good jet separation,
- good electron to hadron discrimination both for isolated electrons and electrons in jets.

An e/h ratio equal to unity minimizes the systematic error in the Q^2 measurement. In comparison to a conventional hadron calorimeter with e/h = 1.2 to 1.4 and an energy resolution of $\sigma(E)/E > 50\%/\sqrt{E} \oplus 5\%$, the proposed energy resolution increases the number of well-measured charged current events by a factor of 1.7, the measurable Q^2 range by a factor of 1.5 and permits access to the very low x region ($x \sim 0.01$). The choice of scintillator readout with photomultipliers offers additional advantages:

- the pulses can be kept shorter than the bunch crossing time of 96 ns so pileup effects are avoided,

* Supported by BMFT.
** Supported by NSERC.
+ Supported by CAICYT.

- the timing of all pulses can be determined to within a nanosecond, this being important for the suppression of an estimated cosmic background of 5 kHz,
- a modular construction is possible, facilitating the installation and calibration,
- the noise can be kept at a low level per readout channel, typically 10 MeV or smaller.

Previous experimental measurements [2] have shown that a depleted uranium–scintillator calorimeter achieves $e/h = 1$ and an energy resolution of $35\%/\sqrt{E}$, provided the thickness of the uranium and scintillator plates is correctly chosen [3,4]. In this article we would like to show that this performance is also achieved by the ZEUS forward calorimeter prototype, constructed according to the same mechanical design as the final calorimeter modules. Particular emphasis is placed on the requirements for calibration and uniformity necessary to achieve an optimum performance.

2. Overview of the ZEUS calorimeter

The ZEUS high resolution calorimeter surrounds the solenoid and tracking detectors hermetically, as shown in fig. 1. The solid angle coverage is 99.8% in the forward hemisphere and 99.5% in the backward hemisphere. Mechanically the calorimeter divides into 3 main components:

- the forward calorimeter (FCAL) covering polar angles from $\theta = 2.2°$ to 39.9°,
- the barrel calorimeter (BCAL) extending from $\theta =$ 36.7° to 129.2°,
- the rear calorimeter (RCAL) extending from $\theta =$ 128.1° to 176.5°.

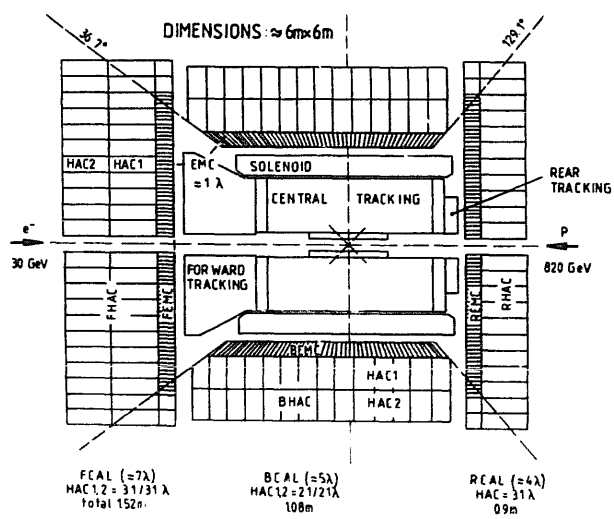

Fig. 1. Longitudinal cut of the ZEUS central detectors along the beam axis. The 3 components of the uranium scintillator calorimeter (FCAL, BCAL, RCAL) are shown. The lines indicate the segmentation of the readout.

The structure of the 3 calorimeter components is similar. They are subdivided longitudinally into 2 parts. The inner part constitutes the electromagnetic calorimeter (EMC) with a depth of about $26X_0$ (or 1λ for hadronic interactions). The outer part is called the hadronic calorimeter (HAC). It varies in depth from 6λ in the very forward region to about 3λ in the rear region. In both FCAL and BCAL the HAC is read out in 2 sections (HAC1 and HAC2). The planes of division are nonprojective except for the electromagnetic part of the BCAL.

The sampling thickness has been chosen to be $1X_0$, leading to depleted uranium (DU) plates 3.3 mm thick *. The DU plates are fully encapsulated by a stainless steel foil of 0.2 mm thickness in the EMC and 0.4 mm in the HAC. The steel foil allows a safe handling of the uranium plates during construction and at the same time its thickness serves to adjust the signal from the DU natural radioactivity. This signal has to be low enough to keep the photomultiplier background current and the noise small, yet high enough to provide an accurate calibration. The scintillator (SCI) thickness has been chosen to be 2.6 mm in order to achieve $e/h = 1$, according to measurements and Monte Carlo calculations [2–4].

Each calorimeter section is read out on both sides (right and left) by wavelength shifter plates (WLS), light guides (LG) and photomultipliers (PM).

3. Mechanical design of the FCAL modules

A three-dimensional view of a maximum size FCAL module in shown in fig. 2. The main elements are listed below (see also fig. 3a and 3b).

- A 4700 mm long T-beam or back which supports the mechanical tensioning elements, the light guides, the photomultipliers and the front end electronics.
- An upper and a lower box profile beam of 2100 mm length (C-legs) screwed to the back beam to which the absorber plates are clamped.
- A 15 mm thick aluminum front plate.
- DU plates which are 4600 mm long, clad with stainless steel foil 0.2 mm thick in the EMC and 0.4 mm thick in the HAC. The EMC sections contain 25 DU plates and each one of the HAC sections 80 DU plates.
- SCI tiles of dimensions 50×191 mm^2 in the EMC, 200×186 mm^2 in the HAC1 and 200×181 mm^2 in the HAC2, interleaved with the DU plates. The 200×200 mm^2 section is called a tower.

* The DU contains 98.4% of U238, 0.2% of U235 and 1.4% of Nb. Its density is 18.5 g/cm^3.

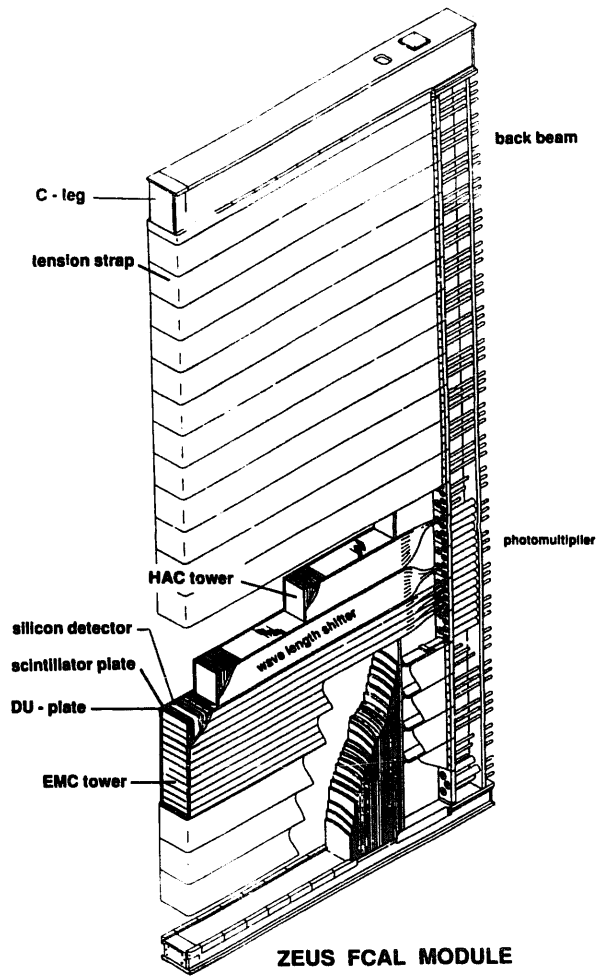

Fig. 2. View of a full size FCAL module.

- Spacers separating the DU plates, in order to avoid any pressure on the scintillator. The spacer area varies from 5×6 mm^2 in the EMC to 5×10 mm^2 in the HAC.
- WLS plates and light guides for the optical readout of the calorimeter towers.
- Photomultipliers mounted to the back beam.
- Stainless steel tensioning straps, 0.3 mm thick, which hold the module compressed.
- Arrays of 10 cm^2 silicon diode detectors mounted in two 15 mm deep gaps * after DU layers 3 and 6 of the EMC, in order to improve the electron–hadron separation.

The DU weight of the module is 8.9 t, the scintillator weight 0.4 t and the total weight including the iron frame 11.9 t.

The measurements which are presented in this article were obtained with 4 prototype modules built according to this mechanical design but consisting of only 4 towers instead of 23 as for the module presented in fig. 2. The mechanical tolerances achieved in the construction of these modules were:

- DU plate thickness: 3.3 ± 0.15 mm, DU plate straightness: ± 0.25 mm,
- steel cladding thickness: 0.2 ± 0.01 mm (EMC), 0.4 ± 0.02 mm (HAC),
- SCI tile thickness: 2.6 ± 0.30 mm, SCI tile transverse tolerances: ± 0.20 mm,
- WLS plate thickness: 2.0 ± 0.20 mm,
- typical construction and stacking tolerances: below 0.5 mm.

The spacers are made from tungsten-carbide * and are located every 20 cm, at the 4 corners of each tower (see fig. 3a). These spacers can support forces up to 2000 N/mm^2. The cross-section of the tensioning straps was fixed at 196×0.25 mm^2. Extensive tests showed that they could be easily operated at a stress of 1500 N/mm^2, almost a factor 4 above the required limit. Detailed finite element calculations have been performed to check the validity of the mechanical design. These calculations indicate maximum forces of 200 N per spacer from accelerations produced during transport and installation of the modules. These forces are compatible with the mechanical design.

Spacers, tensioning elements, WLS and LG assemblies introduce inhomogeneities and dead space, as shown in fig. 3b. The dead space due to the spacers is 0.3% in the EMC and 0.45% in the HAC. The spacer columns do not project to the interaction region and their extension is small compared to the Molière radius of 20 mm in the calorimeter. WLS, LG and tolerances between the modules occupy a volume of 5% in the EMC, 7.5% in the HAC1 and 10% in the HAC2. As they represent low Z materials, no important absorption of energy is expected in these regions. The study of these inhomogeneities and their effect on the calorimeter response was one of the main goals of the measurements with the prototype modules.

4. Optical readout of the FCAL modules

Each tower has a cross-section of 20×20 cm^2 (see fig. 2). The EMC part of the tower is divided in the transverse direction into 4 sections of 5×20 cm^2 and the HAC part is divided longitudinally into 2 sections (HAC1 and HAC2). Each section is read out on the right and left sides by a WLS plate followed by a LG and a PM. The readout from both sides is needed to achieve good transverse uniformity and improves the spatial resolution by "light division". In addition it

* The gap was 10 mm deep for the prototype.

* Spacers of lower Z materials like Si–Al–O or Ti–C compounds are used in the EMC of the final modules.

provides some redundancy useful for cross-checking purposes. The optical readout aims for a uniformity of ±2% both transverse over the SCI tiles and longitudinally along the WLS plate.

As scintillator, SCSN-38 [5] has been selected. This polystyrene-based scintillator has been extensively used in previous tests and showed good stability against aging and radiation [6], high light yield and low signal saturation * [1]. Each scintillator tile was saw cut, polished on all edges and wrapped in Tyvek paper [7] printed with a black pattern to improve the readout uniformity. The pattern used for the EMC tiles is shown in fig. 4a. The uniformity achieved before and after including the printed pattern, as measured with a ruthenium source, is displayed in figs. 4b and 4c, respectively.

The material used for the WLS plates was polymethyl methacrylate (PMMA), doped with a fluorescent dye and UV absorbant up to 360 nm. After performing several uniformity, light yield and radiation resistance tests, Y7 [8] in a concentration of 45 ppm (30 ppm) for EMC (HAC) sections was selected as wavelength shifting agent. The uniformity along the WLS was achieved by an end and a back reflector both made from aluminum foil as shown in fig. 5a. The WLS uniformity before and after correction is presented in fig. 5b. The thickness of the WLS plates was 2 mm.

The light emitted by the WLS is guided to the PM by an adiabatic LG over a distance which varies from 0.25 m for HAC2 sections to 1.65 m for EMC sections. This LG is shaped to match the rectangular cross-section of the WLS to the circular surface of the PM photocathode, via bent strips. PMMA doped with UV absorbant at 450 nm was selected as LG material for the prototype. In the final modules the WLS and LG are made from one WLS plate without glue joints. The measurement of the effective light yield achieved with this optical readout was also one of the goals of the prototype test.

The WLS plates were cut, polished and glued to the LG bent to the appropriate shapes and inserted in a 0.2 mm thick stainless steel cassette, as shown in fig. 5c. Each cassette contains the readout for one side of a full tower (4 EMC and 2 HAC sections). It also incorporates 2.6 mm diameter pipes where radioactive sources can slide in order to monitor the WLS longitudinal uniformity. The WLS plates are pressed against the SCI tiles by foam rubber, but direct contact is avoided by 0.4 mm diameter nylon fishing lines. Towards the PM side, a 'pig-tail' connecting an optical fibre for light injection is glued to the LG. Tests with radioactive sources and light injection with a laser and LEDs have been performed with the prototype modules but the results will not be presented in this article.

After extensive tests [1], the Valvo XP1911 and the Hamamatsu R580 photomultipliers were selected for EMC and HAC sections, respectively, in the final FCAL modules. The prototype modules were equipped with the XP2972 and XP2081 types, both from Valvo, for EMC and HAC sections, respectively. The PMs were equipped with standard resistive bases. As a result they have been heated during the test up to 35 °C, causing gain instabilities and an increased dark current. For the final modules the PM HV is supplied by a low-power Cockcroft–Walton generator [1], in order to minimize heat dissipation and safety hazards.

5. Experimental setup

The 4 prototype modules were assembled at York University (Canada) and tested in the T7 beam of the CERN-PS with particles in the momentum range of 1 to 10 GeV/c, and in the X5 beam of the CERN-SPS with particles in the momentum range of 10 to 100 GeV/c. These 4 modules form a 7λ deep and 80×80 cm^2 cross-section calorimeter, as shown in fig. 6a. The main

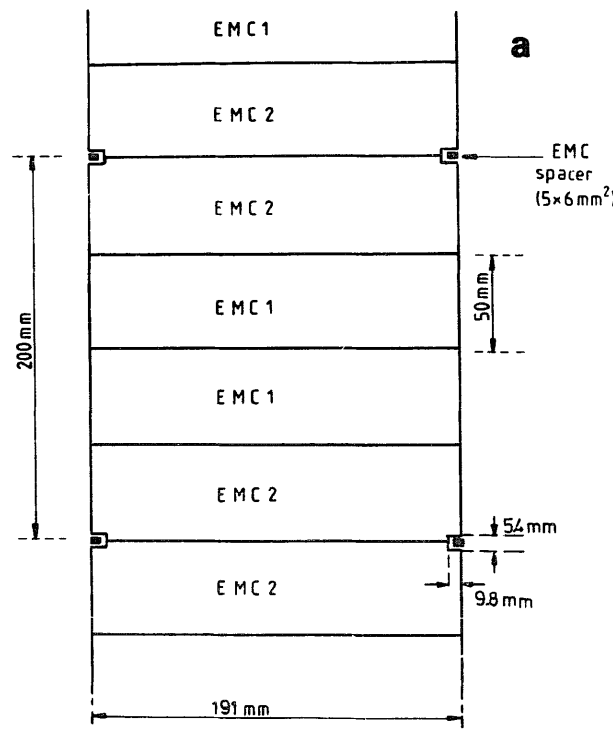

Fig. 3. (a) Spacer and scintillator arrangement in the EMC. (b, see next page) Cut showing the layer structure of a FCAL module, a) front part of the stack, b) EMC-HAC1 transition, c) HAC1-HAC2 transition, d) back part of the stack. The gap for the silicon detectors is 10 mm deep for the prototype modules, but 15 mm deep for the final modules.

* The KB parameter appearing in Birk's law has been measured by us to be KB = $(0.84 \pm 0.01)10^{-2}$ g/(cm^2 MeV).

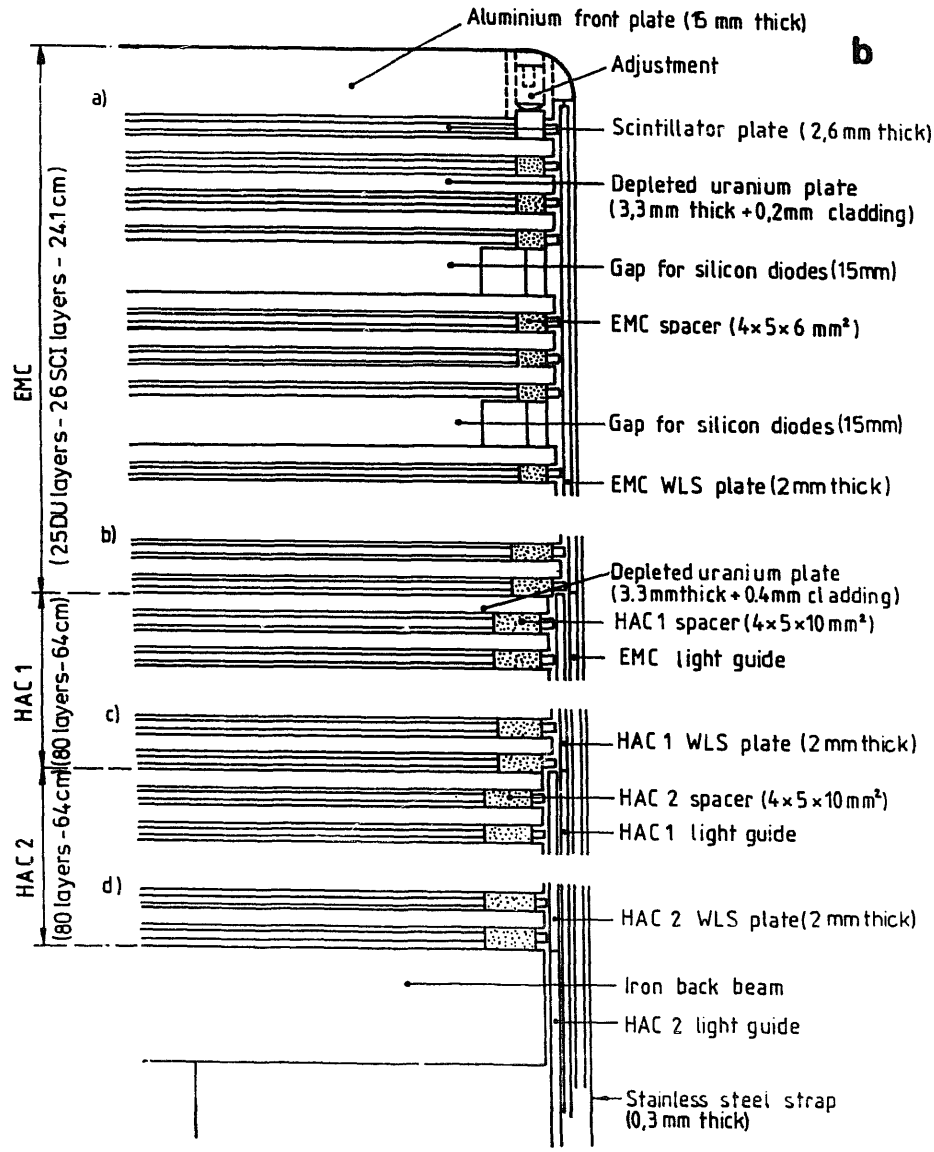

Fig. 3. (continued).

parameters of this calorimeter are summarized in table 1. The tower and EMC section numbering is also indicated in fig. 6a.

The experimental setup in the beamline is shown in fig. 6b. It consists of 5 scintillation counters (B1 to B5) used to define the beam, and two Cherenkov counters (C1 and C2) used for particle identification. The dimensions of the B1 and B2 counters were 10×10 cm^2, B3 was a 5 mm wide counter used whenever a narrow and well-localized beam was needed, finally B4 was a 20×20 cm^2 veto counter, with a 1 cm diameter hole in the middle, used to reject beam halo particles. The B5 counter located behind the calorimeter was used to trigger on muons. Both Cherenkov counters were filled with CO_2 at the PS beam and with helium and nitrogen respectively at the SPS beam. In all cases the pressure was set below the pion threshold for electron–hadron discrimination *. Typical trigger conditions are also indicated in fig. 6b. The narrow counter B3 was taken out of the trigger whenever high rates were required, namely for calibration, energy scan and muon runs. This counter was mainly used for uniformity scans of the calorimeter.

The calorimeter was installed on a movable stand allowing both horizontal and vertical translations. The

* In the high-energy X5 beam, a clean hadron beam was obtained by putting a $1X_0$ converter at the position of the intermediate focus. A clean electron beam was obtained by sweeping charged particles with a magnet and converting the resulting neutral beam in a lead foil a few meters downstream of the target.

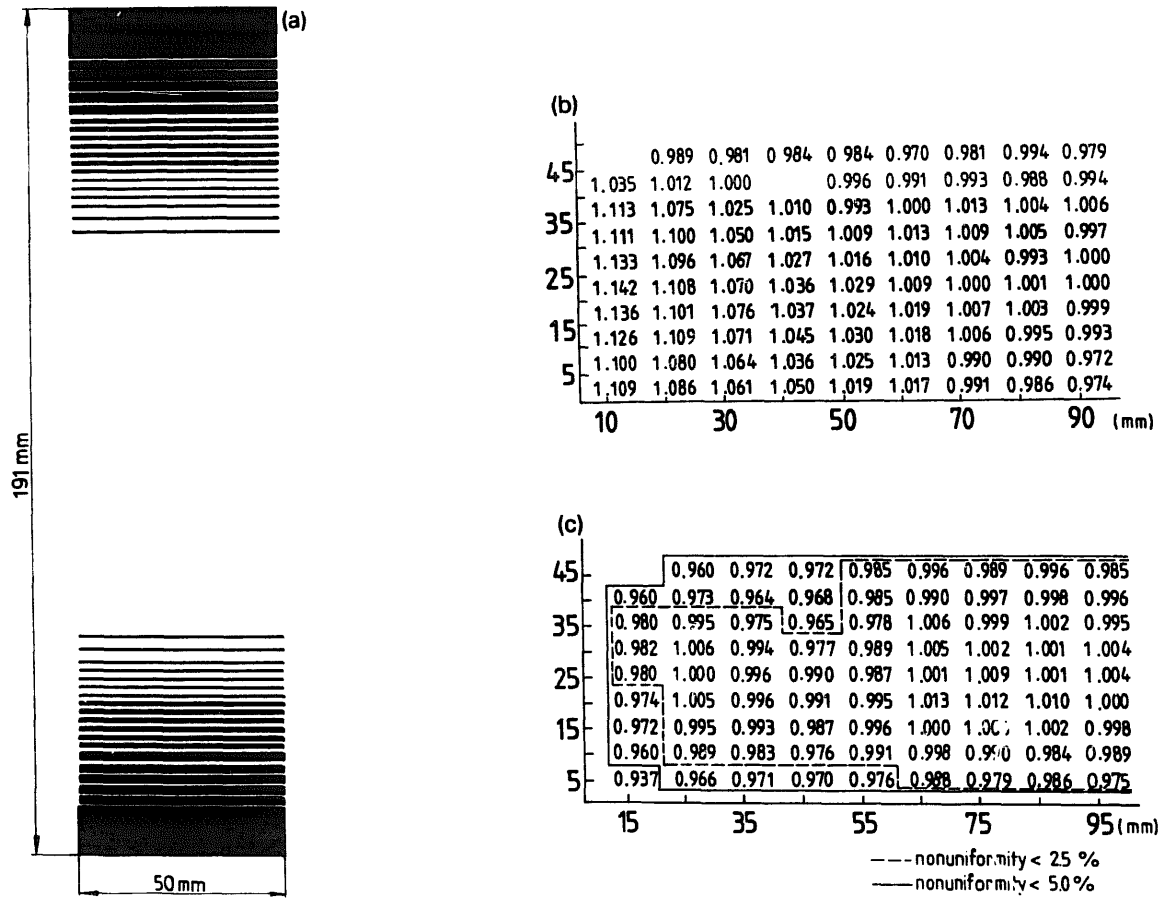

Fig. 4. (a) Printed black pattern used to correct the nonuniformities of a EMC scintillator tile. Uniformity of a EMC scintillator tile, (b) before correction, (c) after correction, as measured with a ruthenium source.

Table 1
Main parameters of the prototype calorimeter

	EMC	HAC
Absorber material	depleted uranium (DU)	
Absorber cladding	stainless steel	
Readout material	SCSN-38 scintillator (SCI)	
DU thickness	3.3 mm	3.3 mm
Cladding thickness	0.2 mm	0.4 mm
SCI thickness	2.6 mm	2.6 mm
Effective X_0	7.4 mm	7.6 mm
Effective λ	210 mm	207 mm
Effective R_M	20.2 mm	20.0 mm
Effective density	8.7 g/cm^3	8.7 g/cm^3
Transverse segmentation	5×20 cm^2	20×20 cm^2
Longitudinal segmentation	$25.9X_0$ (0.96λ)	HAC1 (3.09λ) HAC2 (3.09λ)
Total length	24.1 cm	128.0 cm
Total cross-section	80×80 cm^2	80×80 cm^2
Optical readout	2 mm thick WLS plates + light guides	
WLS material	PMMA + Y7 (45 ppm)	PMMA + Y7 (30 ppm)
Photomultipliers	XP2972 (Valvo)	XP2081 (Valvo)
Readout channels	128	64

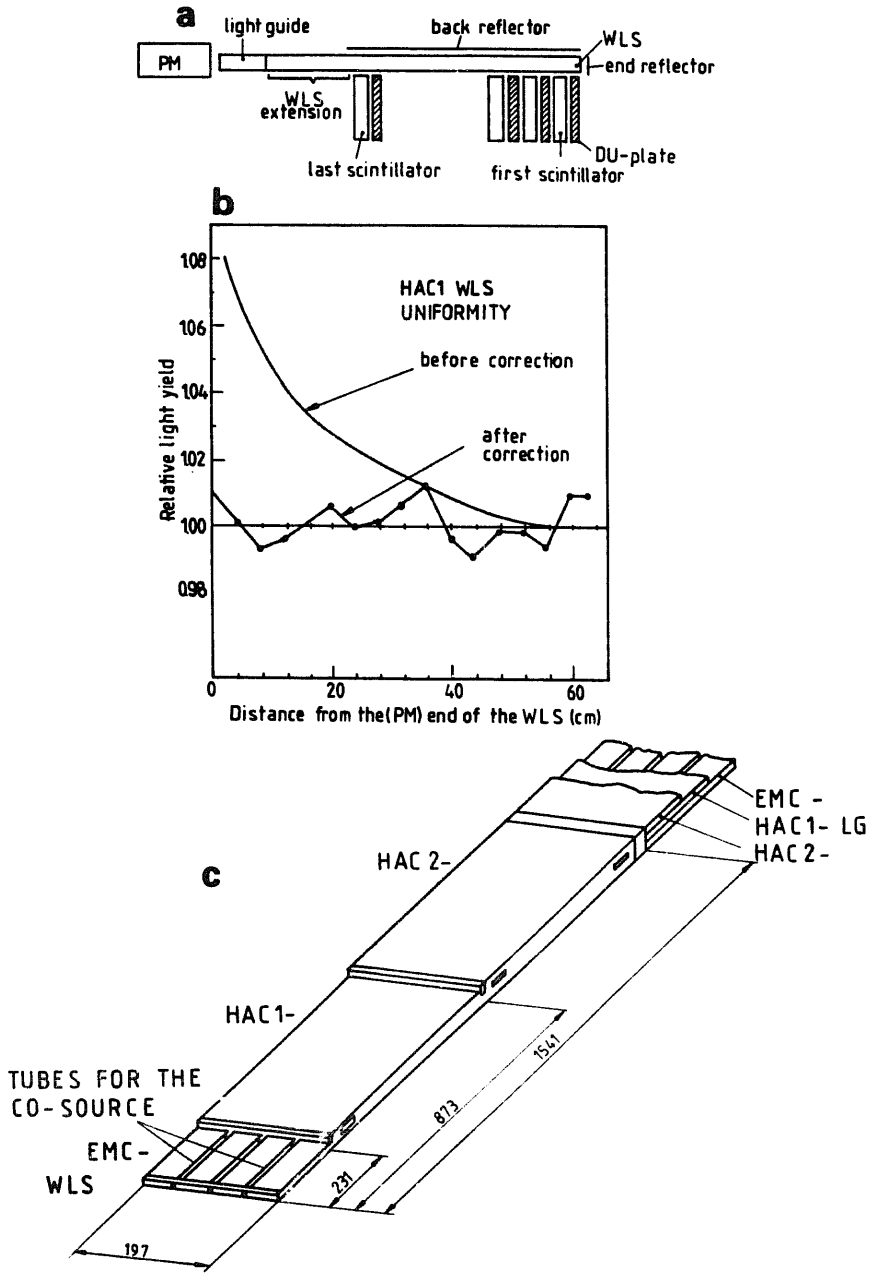

Fig. 5. (a) Schematic view of the WLS readout. (b) Uniformity of a HAC1 WLS plate, before and after correction, as measured with a ruthenium source. (c) Assembly inside a cassette of the different components used for the optical readout.

incident position of the beam on the calorimeter could be located with a precision of about 2 mm in the horizontal direction and 1 mm in the vertical one. The stand could also be rotated in order to vary the angle of beam incidence.

The calorimeter was read out by a total of 192 PMs. The PM signals were digitized by charge integrating ADCs (2282B from LeCroy) and read out by a Motorola-68K/VME based computer at the PS and by a PDP-11 computer at the SPS. The integration gate for normal events was 100 ns. We note that the electronics used in this test differs considerably from the final electronics which shapes the PM pulses and then samples them every 96 ns [9]. This final electronics also provides a timing of the pulses with an accuracy better than 1 ns. This timing feature was not available for the measurements reported here.

6. Calibration

6.1. Calibration with uranium radioactivity

An important advantage of uranium calorimeters is the possibility to use the uranium natural radioactivity

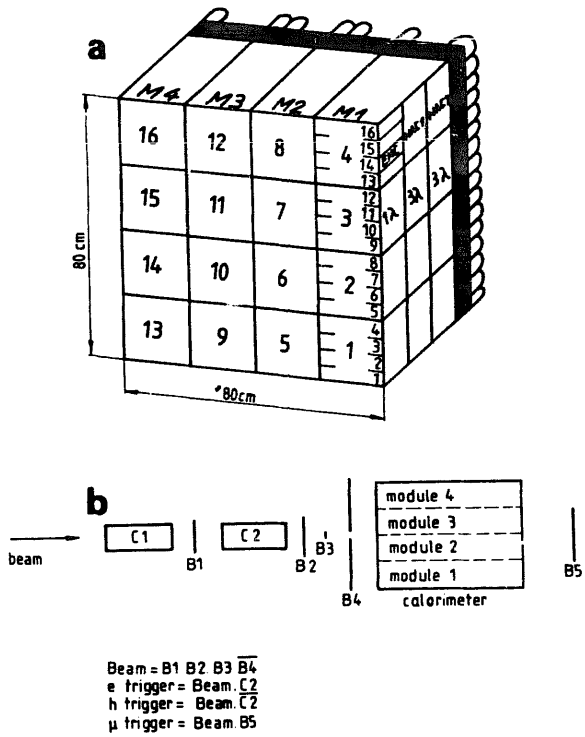

Fig. 6. (a) View of the prototype calorimeter modules showing module, tower and section numbering. (b) Experimental setup in the beamline.

for calibration purposes [2]. The quality of this calibrations has been extensively investigated with the prototype modules.

The PM current induced by the uranium radioactivity was measured with integrators as indicated in fig. 7a. The time constant of integration was set at about 1 s. The signal was then digitized by the ADC with an integration gate which could be increased to 10000 ns and which was used to tune the final value of the signal (UNO signal) in ADC channels. The integrator part of the circuit could be disabled for normal events by computer control.

At the PS the HV of the PMs was tuned in such a way that the signal from 5 GeV/c electrons corresponded to 125 pC (500 ADC channels). The current induced by the uranium radioactivity was then 0.6 μA for EMC tubes. At the SPS the 30 GeV/c electron signal corresponded to 1000 ADC channels and the induced currents were consequently reduced by a factor 3. The HV of the HAC tubes was set to have a current from the uranium radioactivity of 3.0 μA, giving approximately the same charge per deposited energy for EMC and HAC sections (see section 6.3). By tuning the ADC integration gate, the final UNO signals were kept at constant values of about 300 and 1500 ADC channels for EMC and HAC tubes respectively. Figs. 7b and 7c display typical UNO distributions. The width of these distributions is about 1 ADC channel, corresponding to 0.7 nA for the SPS adjustment of EMC tubes.

The UNO signal was used to study and correct the PM gain variations as a function of time. We defined the following two quantities (see fig. 8a):

- δ = UNO variation between 2 consecutive runs for a given PM,
- Δ = maximum UNO variation during the period of measurements for a given PM.

Fig. 8b displays the UNO signal for a well-behaved tube as a function of time. The UNO measurements were performed every 2 hours during a period of ap-

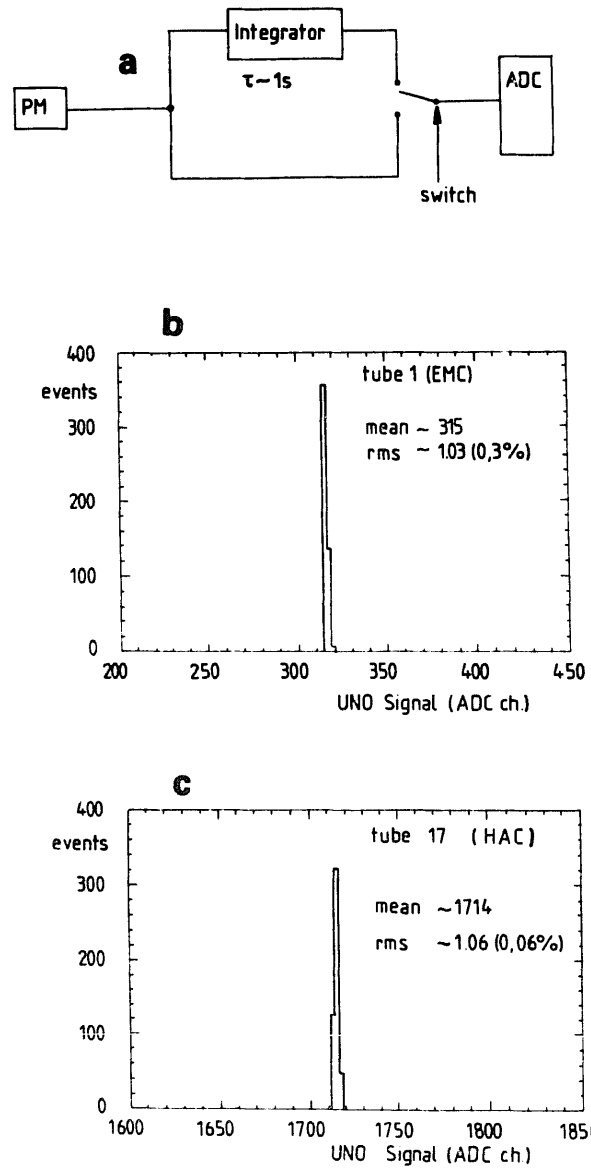

Fig. 7. (a) Electronic circuit used in the test. The integrators are used to measure the current induced by the uranium radioactivity (UNO signal). (b) UNO signal measured in a typical EMC channel. (c) UNO signal measured in a typical HAC channel.

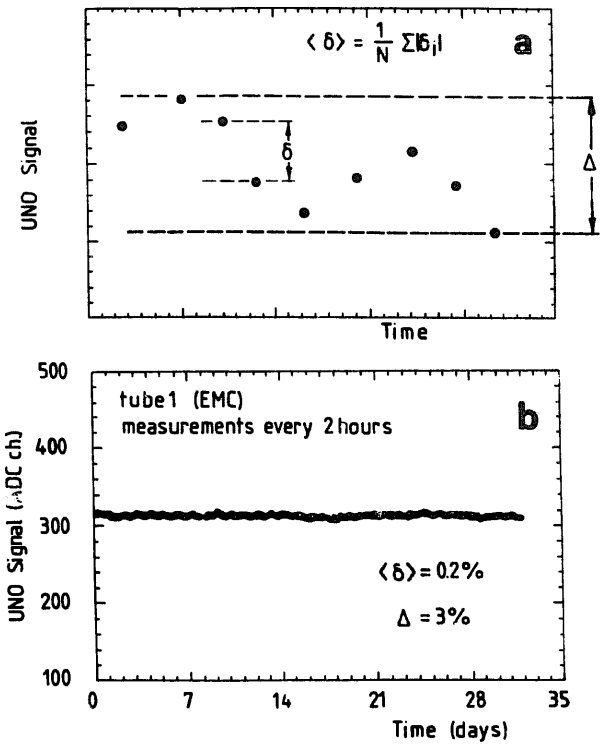

Fig. 8. (a) Definition of short (δ) and long (Δ) term variations of the UNO signal. (b) UNO signal variations for a well-behaved channel. The measurements were performed every 2 hours during a period of 30 days.

Table 2
Short ($\langle\delta\rangle$) and long (Δ) term variations of the UNO signal. The values are averages over all EMC and HAC tubes. The frequency of the measurements is indicated for the short term variations

	$\langle\delta\rangle$ [%] 2 hours	$\langle\delta\rangle$ [%] 8 hours	$\langle\delta\rangle$ [%] 24 hours	Δ [%] 30 days
EMC	0.5	0.7	1.0	9.5
HAC	0.1	0.2	0.3	3.7

proximately 30 days. On the average, the short term variations for the tube of the figure are $\langle\delta\rangle = 0.2\%$ and the long term variations $\Delta = 3\%$. These variations differ considerably from channel to channel. The quantities $\langle\delta\rangle$ (for measurements performed every 2 hours) and Δ (after 30 days of running) are plotted for all calorimeter tubes in fig. 9a to 9d. Short term variations are typically below 1% whereas long term variations are typically 10%. The short term variations depend on the frequency of the measurements. In table 2 we report the average values for measurements performed every 2, 8 and 24 hours. We conclude that measurements every 8 hours are sufficient to monitor the UNO signal with 1% accuracy.

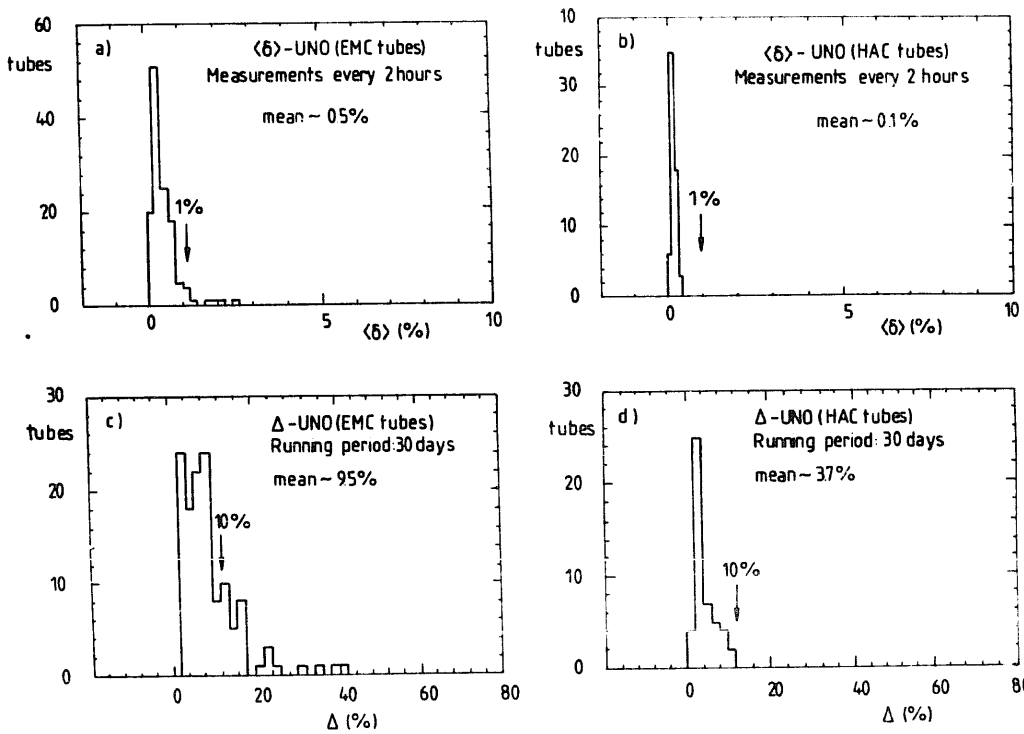

Fig. 9. Stability of the UNO signal. Shown are the short and long term variations for all EMC (a and c) and all HAC (b and d) channels. The short term variations were obtained for measurements performed every 2 hours. The long term variations correspond to 30 days of running.

6.2. Uranium radioactivity versus beam calibration

The variations observed in the UNO signal are of course caused by the PM gain variations but might also be caused by changes in the PM dark current. In order to study the ability of the UNO signal to detect real gain variations we have traced them also with muons and electrons and we have compared the variations in the average electron and muon response (e and μ) to the UNO variations. For this purpose the whole calorimeter was scanned 5 times with a 5 GeV/c electron beam incident at the centre of each EMC section and with a 5 GeV/c muon beam incident at the centre of each HAC section. The spread of the 5 e/UNO or μ/UNO ratios for a given EMC or HAC tube, respectively, gives the quality of the UNO calibration. These spreads are plotted for all channels in fig. 10a to 10c. The average spread of e/UNO ratios for EMC tubes is 1.1% and the average spread of μ/UNO ratios for HAC tubes is about 0.5%. These values include a variety of

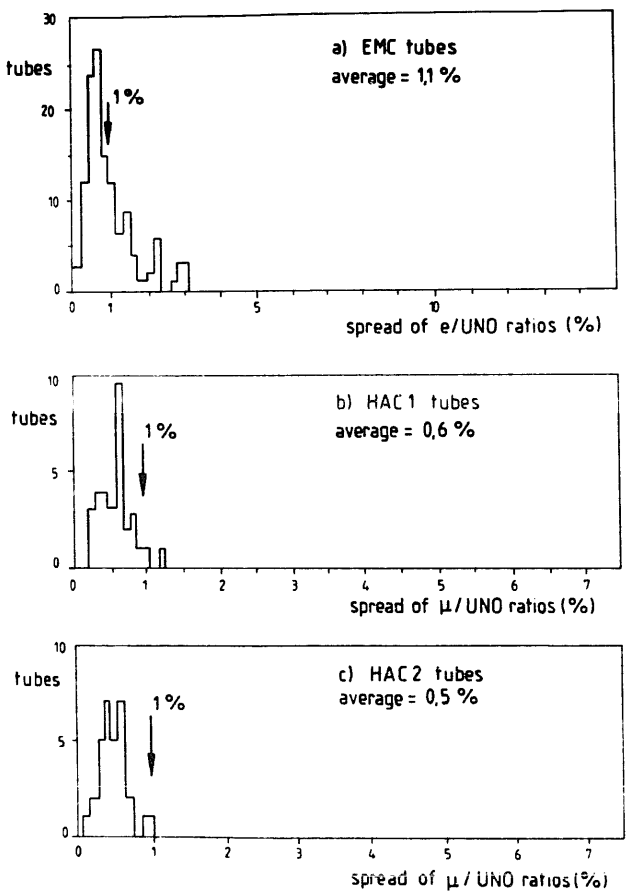

Fig. 10. Capability of the UNO signal to detect PM gain variations. Shown are the spread of a) e/UNO ratios for EMC tubes, b) μ/UNO ratios for HAC1 tubes, c) μ/UNO ratios for HAC2 tubes. These spreads were obtained after 5 calibration cycles of all calorimeter sections with 5 GeV/c electrons or muons.

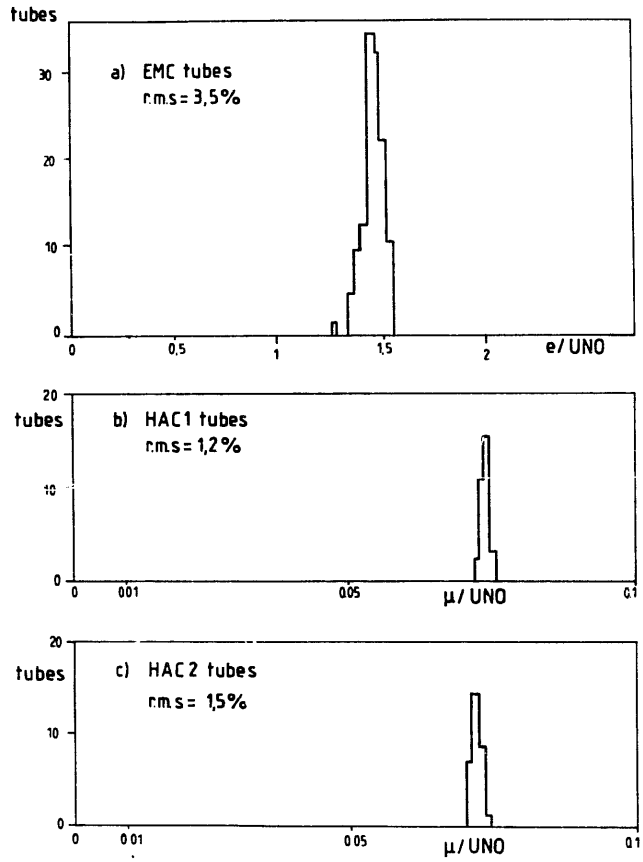

Fig. 11. Ratio of UNO and beam calibration constants for all calorimeter channels; a) e/UNO ratios for EMC tubes, b) μ/UNO ratios for HAC1 tubes, c) μ/UNO ratios for HAC2 tubes. These ratios have been corrected by imposing the same average value for all modules and for right and left tubes.

small effects like statistical errors, shifts due to the calorimeter positioning, etc., but allow us to conclude that the UNO signal is able to trace PM gain variations within 1% accuracy.

The UNO signal can be used not only to trace PM gain variations, but also to intercalibrate the gain of the PMs by balancing the values for tubes in the same calorimeter sections (EMC, HAC1 or HAC2). The quality of this calibration can be checked by comparing e and μ to UNO values for different tubes. The e/UNO ratios * for EMC tubes are plotted in fig. 11a. The μ/UNO ratios for HAC1 and HAC2 tubes are plotted respectively in fig. 11b and 11c. The widths of these distributions are summarized in table 3. There are two

* Four EMC tubes showing abnormally low e/UNO ratios have been excluded. These tubes had a significant dark current, which is very sensitive to temperature changes. Replacing the passive bases by Cockcroft–Walton bases will reduce the PM temperature by about 15°C, thus removing this effect.

Table 3
Difference between the UNO and the beam intercalibration of the calorimeter channels. In the second row the average ratios per module have been balanced and the average R and L ratios as well. In the third row only sums of right and left tubes have been considered

	EMC e/UNO [%]	HAC1 μ/UNO [%]	HAC2 μ/UNO [%]
No corrections	4.3	2.3	4.1
With corrections	3.5	1.2	1.5
R+L	2.4	1.1	1.2

possible causes for the discrepancy between the beam and the UNO calibration:
- mechanical effects which can affect the UNO signal (like thickness tolerances) or the beam signals (small translations or rotations of the modules),
- dark current effects which affect exclusively the UNO signal.

The effects of the first kind are almost completely removed by imposing module by module the same average ratios and also that the PMs of the left side deliver on the average the same ratios as the PMs of the right side. As shown in table 3 this correction removes part of the discrepancy but still this discrepancy is larger than 1%, even if the sums of right and left PMs are performed for each section.

We conclude that the UNO signal provides a valuable intercalibration of the PM gains at the 2 to 3% level of accuracy, but a calibration to within 1% has only been achieved up to now with beam particles.

6.3. EMC–HAC intercalibration

The UNO signal can be used to intercalibrate geometrically identical sections but it is more difficult to use for intercalibration between EMC and HAC sections. A rough estimation which takes into account the size and number of scintillator layers and the UNO signal reduction due to the difference in cladding, predicted a ratio of about 5 between the UNO signal in the HAC and in the EMC sections. This ratio was used for a first PM gain tuning but other methods had to be derived for a more precise calibration.

We defined the intercalibration parameter α in the following way: $E = E_{EMC} + \alpha E_{HAC}$, where E_{EMC} and E_{HAC} are the energy deposited in the EMC and HAC sections, respectively. Various (arbitrary) prescriptions can be used to determine α:
- optimal hadron energy resolution,
- equal response for electrons and hadrons,
- muon response proportional to the number of SCI layers, etc.

For a compensating calorimeter these methods are expected to be equivalent. We selected the first prescription and α was determined by requiring the fractional energy resolution for hadrons, σ_E/E, to be minimal. Fig. 12a displays σ_E/E for hadrons of 10 and 100 GeV/c momenta. The following observations can be made:
- the minimum of σ_E/E is more pronounced for higher momenta and therefore the sensitivity of the method is also increased,
- the minimum of σ_E/E depends slightly on the momentum of the incident hadron and therefore the value of α as well.

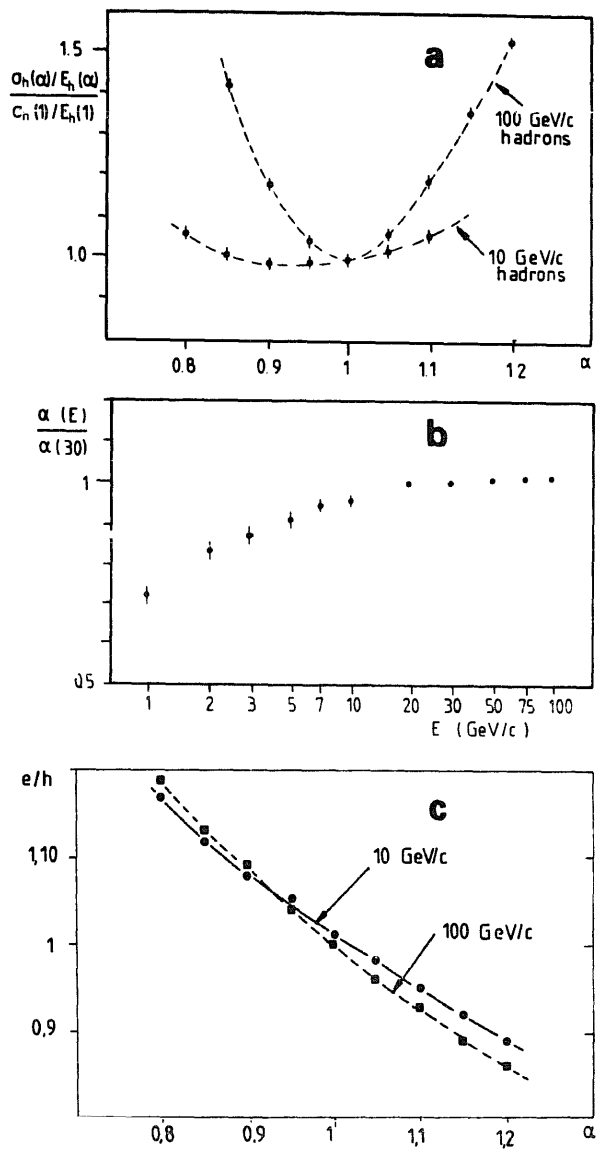

Fig. 12. (a) Fractional energy resolution for 10 and 100 GeV/c hadrons as a function of the intercalibration parameter α. The energy resolutions are normalized to the value obtained for $\alpha = 1$. (b) Intercalibration parameter α obtained by minimization of the hadronic energy resolution as a function of the beam momentum; α is normalized to the value obtained for $E = 30$ GeV/c. (c) e/h as a function of the intercalibration parameter α for 10 and 100 GeV/c particles.

Fig. 12b displays the value of α which minimizes the hadron energy resolution as a function of the beam momentum. No increase is observed above 30 GeV/c. The value of α at 30 GeV/c was then used for the final calorimeter calibration. As discussed in section 9, this value of α meets also the important requirement of providing a ratio e/h of 1 (see also fig. 12c). The final UNO ratio between HAC and EMC sections obtained in this way was 5.40.

We note finally that the ratio between the average 5 GeV/c muon signals in the EMC and HAC sections was measured to be 3.14, compatible with the ratio of scintillator layers, 80/26 = 3.08. However second order corrections are also needed here to obtain a more precise value. These corrections should account for the multiple scattering of muons and the difference in cladding between EMC and HAC sections.

7. Uniformity

The calorimeter uniformity has been extensively studied with electrons and hadrons both at the PS and SPS beams. Three regions of nonuniformities have been identified:

- the boundary between modules *,
- the location of the spacers,
- the boundary between EMC sections.

The first class of nonuniformities is by far the most important one and has been carefully investigated. The result of various scans between the centres of modules 2 and 3, with a 5 GeV/c electron beam incident under angles of θ = 0, 40 and 80 mrad, is presented in fig. 13a to 13c. We observe a big enhancement in the calorimeter response just between the two modules **. This enhancement is reduced as the modules are rotated. Experimental studies (e.g. by blocking the light transfer between the scintillator and the WLS) have shown that it is mainly due to Cherenkov light produced by shower particles travelling through the WLS. It can be reproduced by Monte Carlo calculations using the EGS4 shower generator [10] assuming an efficiency of detection for the energy deposited in the WLS relative to the energy deposited in the scintillator of about 30%. It is interesting to note that such an effect is not present for hadronic showers as demonstrated by fig. 14a to 14c [+]. Therefore hadronic showers are much less sensitive to

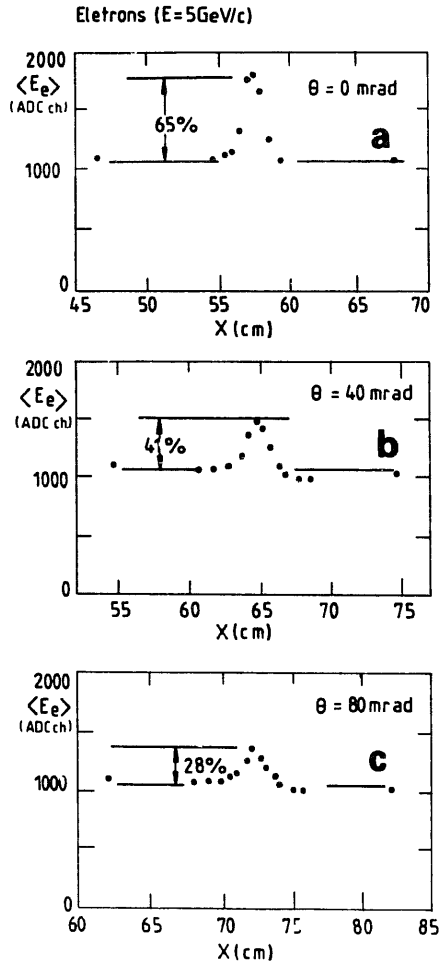

Fig. 13. Calorimeter response to 5 GeV/c electrons as a function of the beam impact position on the calorimeter. The scans were performed between the centres of modules 2 and 3 under angles of incidence of (a) 0 mrad, (b) 40 mrad, (c) 80 mrad.

mechanical details inside the calorimeter than electromagnetic showers and do not cause a significant uniformity problem.

Several solutions have been tried to solve the uniformity problem for electromagnetic showers. The most successful one has been a lead foil introduced between the modules as sketched in fig. 15. The thickness of the lead foil has to be optimized to absorb the right amount of energy in order to compensate for the additional signal detected in the WLS. It has to run along the whole calorimeter depth, since some light is observed by the HAC sections for electrons incident under very small angles. Scans with no lead, 2 and 3 mm thick lead foils were performed with 5 and 30 GeV/c electron beams incident under angles of 0, 40 and 80 mrad. Similar results were obtained for both energies, thus indicating that the nonuniformities are essentially energy independent. The result for the 30 GeV/c scans is presented in fig. 16. We observe that, with a 2 mm thick

* In the ZEUS FCAL the module boundaries are at angles in the horizontal plane of $\theta = 40 + (n-1)80$ mrad, n being the 'crack number'.

** The crack for $\theta = 0$ mrad corresponds in the figure to a horizontal position of $x = 57.5$ cm. This position changes when the modules are rotated.

+ The small dip observed under normal incidence is due to back leakage.

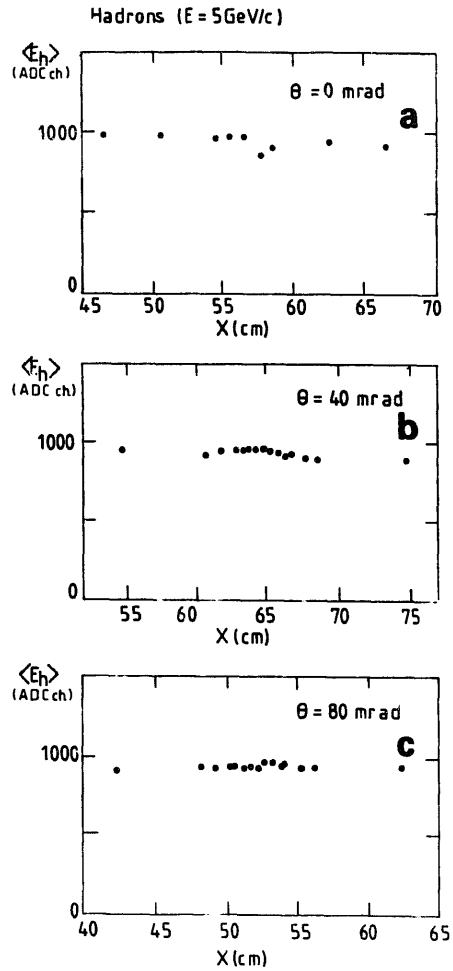

Fig 14. Calorimeter response to 5 GeV/c hadrons as a function of the beam impact position on the calorimeter. The scans were performed between the centres of modules 2 and 3 under angles of incidence of (a) 0 mrad, (b) 40 mrad, (c) 80 mrad.

lead foil, a good uniformity is achieved for $\theta > 80$ mrad and that a dip in the response can be obtained by further increasing the thickness of the lead foil. Again, the lead has little impact in the hadron response as seen in fig. 17. It is interesting to note that the lead foil acts mainly by reducing the response of the HAC sections (see fig. 18). We observe finally that the electron energy resolution is only slightly degraded at the location of the lead for angles of incidence of 80 mrad or larger (see fig. 19).

The average shift in the electron response and its spread over the entire calorimeter have been calculated by extrapolation of the measurements presented in fig. 16. They are displayed as a function of the angle of incidence in figs. 20a and 20b. We conclude from these results that both the average shift and the rms of the electron response distribution can be kept below 1% except for the calorimeter boundary at the smallest angle of incidence (40 mrad).

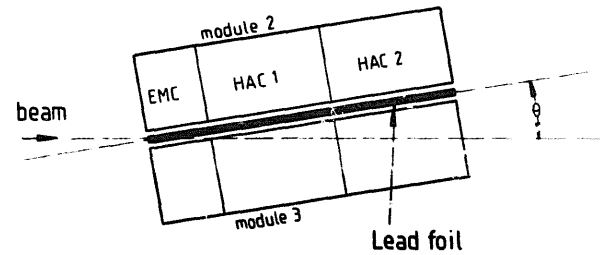

Fig. 15. Schematic drawing showing the location of the lead foil between modules 2 and 3.

As mentioned in section 3, spacers are located at the corner of each 20 × 20 mm^2 tower. At the location of a spacer the electron response is reduced by about 20% (see fig. 21). Although the problem was not studied in full detail, a solution consists of reducing the lead thickness close to the spacers and using lower Z materials in their composition.

Finally nonuniformities of about 5% have been observed at the boundaries between the EMC sections of the prototype modules (see fig. 22). They could be explained by a gap of about 1 mm between these sections. In the final modules this gap is reduced to 0.6 mm. Monte Carlo calculations have shown that the effect should then be reduced to 3%, with additional smearing as the angle of incidence increases.

8. Noise and light yield

The calorimeter noise has been determined by summing all channels for random trigger events. A typical distribution obtained in this way is displayed in fig. 23. There are two different contributions to the noise: the uranium noise and the electronic noise. This second component can be isolated by reducing the HV to 400 V *. The distribution obtained in this way is also displayed in fig. 23. All sources of coherent noise like pickup and the 50 Hz baseline ripple have been eliminated so that the total electronic noise is proportional to the square root of the number of channels. The relative importance of both components depends of course on the PM gain. The rms noise levels obtained during the PS and SPS measurements are reported in table 4. We observe that at the PS the uranium noise dominates whereas at the SPS, after reducing the PM gain by a factor 3, the electronic noise dominates. The uranium noise amounts to 100 MeV if all channels in the 4 modules are summed up and to 25 MeV for a 20 × 20 cm^2 tower. The implications of these noise

* The gain of the PM is negligible for this voltage. The HV is not reduced to 0 in order to minimize the gain changes once it is set back to the nominal value.

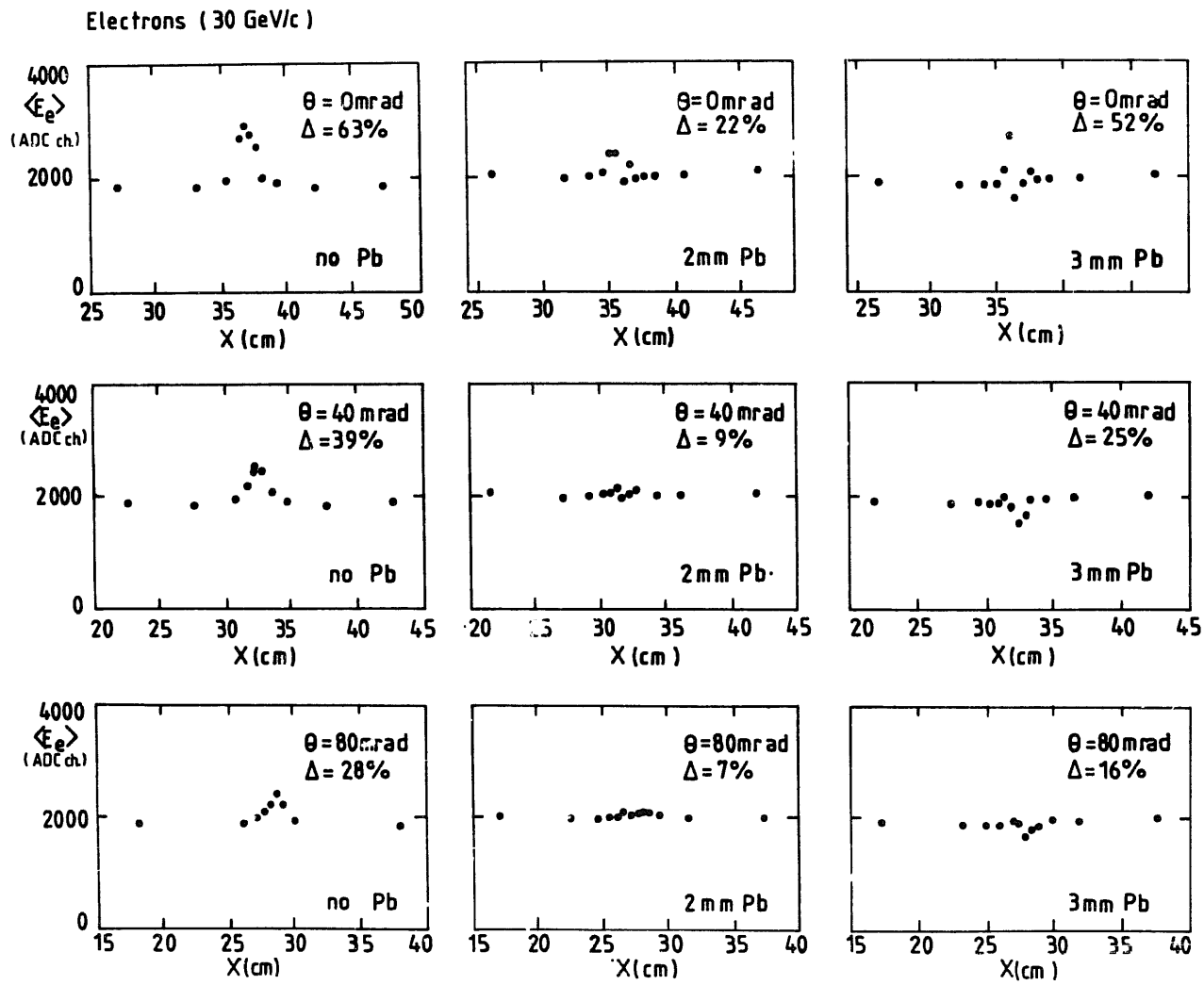

Fig. 16. Calorimeter response to 30 GeV/c electrons as a function of calorimeter position for various angles of beam incidence and thicknesses of the lead foil between modules 2 and 3.

values for the energy resolution will be discussed in section 11.

Each module was equipped with a LED system allowing light injection via an optical fibre close to the photocathode of each PM. The LED output signals were integrated with a 1 μs gate for pulsed LEDs and with a 10 μs gate for LEDs run in the DC mode. Fig. 24 displays two typical LED-DC mode distributions for EMC and HAC tubes. The number of photoelectrons (p.e.) for 1 GeV/c electron equivalent signal (E_0) can be obtained according to the formula

$$N = \left(\frac{E_{\mathrm{led}}}{\sigma_{\mathrm{led}}}\right)^2 \frac{E_0}{E_{\mathrm{led}}},$$

where E_{led} and σ_{led} are the average response and the corresponding rms fluctuation for a given PM. On the average $N = 41.3$ p.e./GeV for EMC tubes and $N = 101$ p.e./GeV for HAC tubes (see table 5). Therefore HAC tubes yield 2.4 times more photoelectrons than EMC tubes. Other methods used to determine the number of photoelectrons (electrons, muons, etc.) gave similar results. The differences in light yield between EMC and HAC sections were investigated and it was found that the light yield depends strongly on the quality of the machining of the WLS pieces *. We note finally that the photoelectron fluctuations of the EMC sections produce a nonnegligible contribution to the total energy

* The light yield of the EMC sections has been increased for the final modules by a factor 2 by improving the polishing of the WLS edges and a tight quality control.

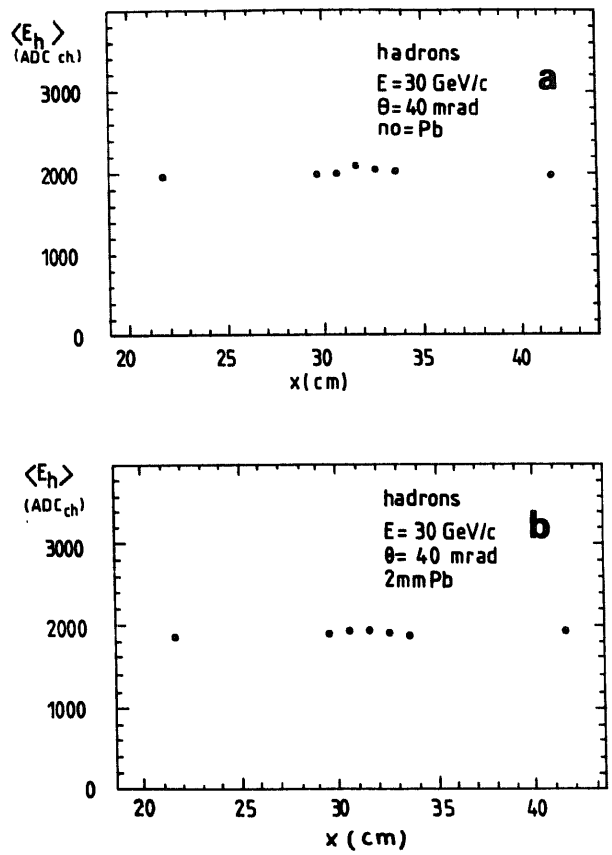

Fig. 17. Calorimeter response to 30 GeV/c hadrons as a function of calorimeter position for a 40 mrad beam incidence and the following setups: (a) no lead between modules 2 and 3, (b) a 2 mm thick lead foil between modules 2 and 3.

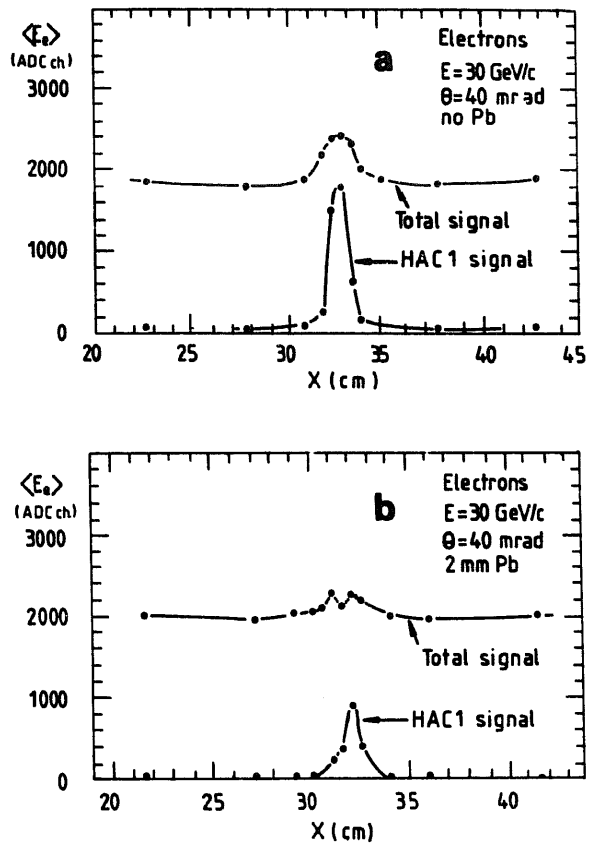

Fig. 18. Contribution of the different calorimeter sections to the 30 GeV/c electrons signal for a 40 mrad beam incidence and the following setups: (a) no lead between modules 2 and 3, (b) a 2 mm thick lead foil between modules 2 and 3.

resolution for electrons ($10\%/\sqrt{E}$ compared to a total value of $18\%/\sqrt{E}$, see next section).

9. Energy resolution and e/h

The calorimeter was exposed to electrons and hadrons in the momentum range of 1 to 10 GeV/c at the PS and 10 to 100 GeV/c at the SPS. At the PS the beam was incident at the centre of EMC section 7 in module 2 (see fig. 6a) and only modules 1, 2 and 3 were read out. At the SPS the beam was incident at the centre of EMC section 7 in module 3 and all 4 modules were read out. At lower energies (PS), the negative polarity of the beam was selected. The beam was therefore composed almost exclusively of electrons and pions. At higher energies (SPS) the positive polarity of the beam was selected in order to increase the particle rates.

Table 4
Total calorimeter noise at the PS (PM high gain) and SPS (PM low gain). All data have been scaled to 4 modules (16 towers)

Noise	PS (high gain) [MeV]	SPS (low gain) [MeV]
Total	104	213
Electronic	48	188
Uranium	92	100

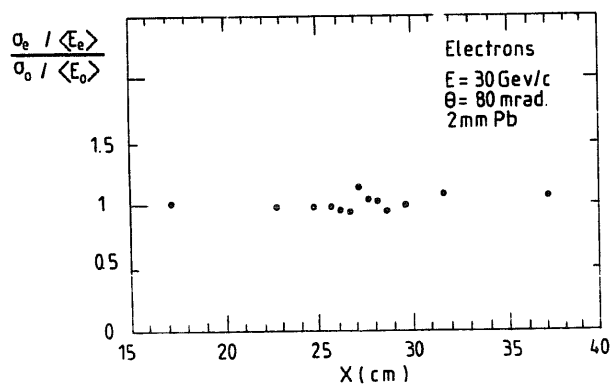

Fig. 19. Energy resolution for 30 GeV/c electrons as a function of the calorimeter position for a 80 mrad beam incidence and with a 2 mm thick lead foil between modules 2 and 3. The fractional resolution is normalized to the value at the centre of the modules.

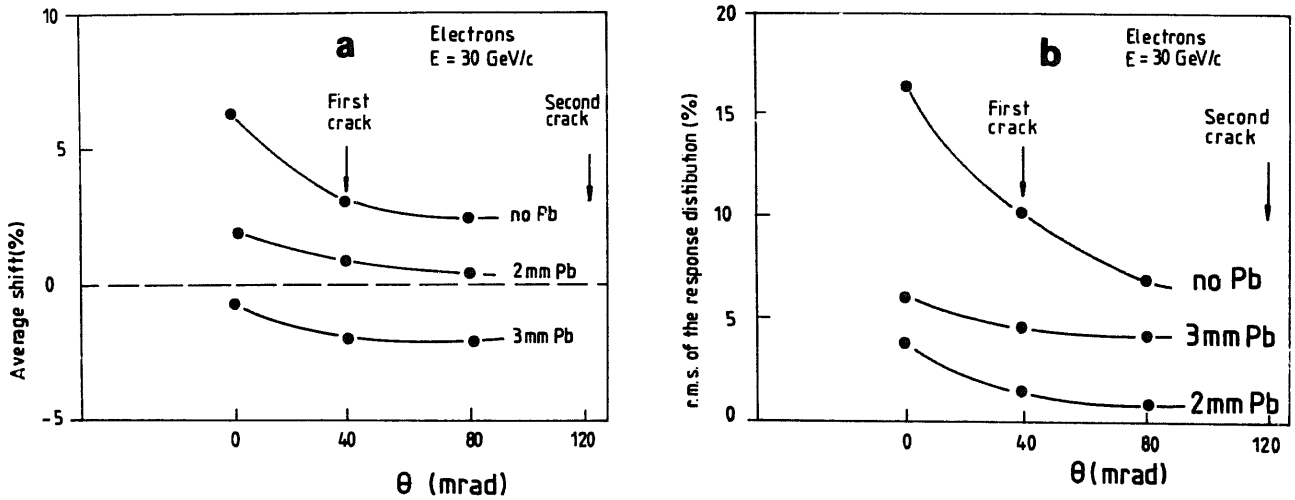

Fig. 20. (a) Shift of the calorimeter response to electrons due to the nonuniformity at a module boundary. The response is averaged over a region of 20 cm around this boundary and presented as a function of angle. The angles of the 2 first ZEUS FCAL boundaries are indicated in the figure. The values were obtained by interpolating the measurements shown in fig. 16. (b) Rms of the response distribution for the same conditions as (a). This value is a direct contribution to the electron energy resolution, for particles entering the calorimeter at random positions.

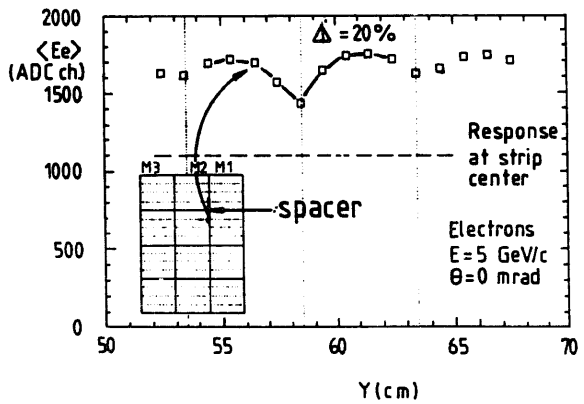

Fig. 21. Calorimeter response to 5 GeV/c electrons as a function of calorimeter position under normal incidence. The scan was performed in the vertical direction between modules 1 and 2.

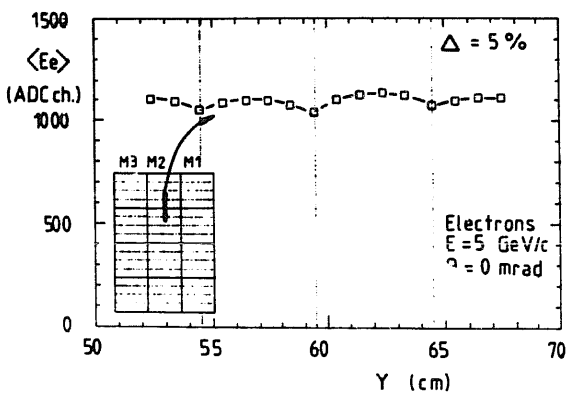

Fig. 22. Calorimeter response to 5 GeV/c electrons as a function of calorimeter position under normal incidence. The scan was performed in the vertical direction at the centre of module 2.

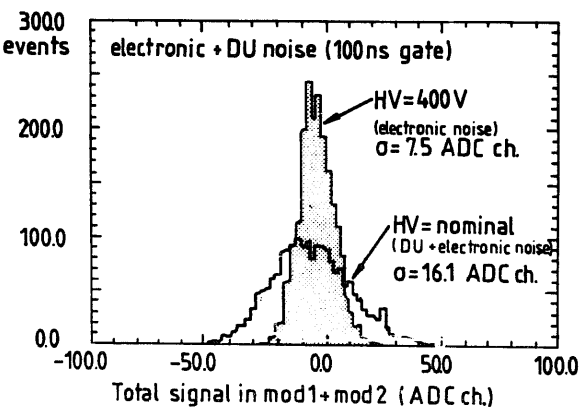

Fig. 23. Sum of all calorimeter channels in modules 1 and 2 for random trigger events (only calorimeter noise) for the two following cases: HV at nominal value (showing electronic and uranium noise) and reduced to 400 V (showing only electronic noise). In both cases the pedestals are subtracted. These measurements were performed at the PS with high PM gains.

Table 5
Average number of p.e. for 1 GeV equivalent electron signal and tube. The average values and spreads are given for the individual modules

Light yield	EMC tubes		HAC tubes	
	Mean	Spread [%]	Mean	Spread [%]
Mod. 1	39.5	33	91.2	15
Mod. 2	33.0	43	92.2	30
Mod. 3	43.0	46	109.5	39
Mod. 4	49.8	21	110.9	27
Average	41.3		101.0	

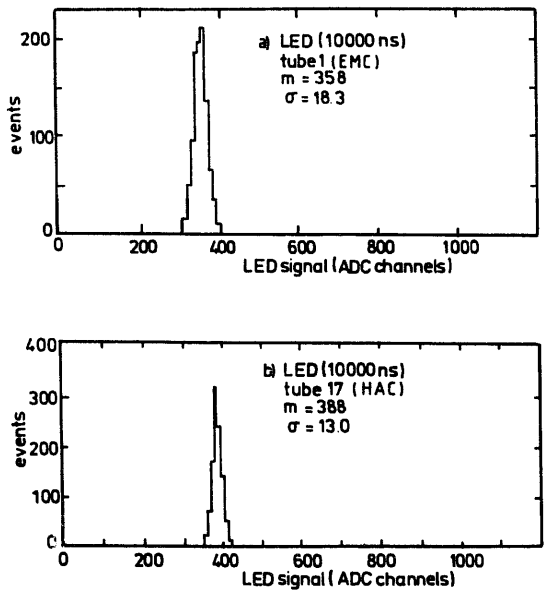

Fig. 24. LED pulse height distributions obtained for an EMC tube (a) and a HAC tube (b). The LEDs were run in the DC mode and the integration time was 10000 ns. There is a small contribution of the uranium noise to the width, which has been subtracted to calculate the light yield.

The hadron content of this beam is dominated by pions around 10 GeV/c and by protons around 100 GeV/c. No separation between protons and pions was attempted.

The events were selected by means of the Cherenkov counters and the signals in the calorimeter itself. The refractive index of the gas in the Cherenkov counters was optimized to have an efficient electron–hadron rejection at the lowest momenta of both beams. At the highest momenta the shower topologies in the calorimeter itself provide a clear enough separation. In this way, samples of electrons and hadrons with contaminations smaller than 1% could be isolated for all beam momenta. For beam momenta above 10 GeV/c we demanded that the energy deposited in the HAC2 sections of the calorimeter did not exceed 10% of the average energy deposited in the whole calorimeter. Otherwise the hadron distributions develop large tails due to leakage at the back of the calorimeter *. This cut suppresses 5% of the events at 10 GeV/c, increasing to 50% at 100 GeV/c.

The resulting electron and hadron distributions for all beam momenta are displayed in figs. 25 and 26 for PS and SPS beams respectively (note the different scales due to the different PM gains). Fig. 27 displays in logarithmic scale the electron and hadron distributions at 30 GeV/c. We observe that they are well described by Gaussian distributions, as expected for a compensating calorimeter. The tail towards low values observed in the hadron distribution is due to leakage at the back of the calorimeter. The results obtained after fitting Gaussian functions to these distributions are reported in tables 6 and 7. These tables contain measured and corrected values for the energy resolution. The corrected values have been obtained by:

- summing only the energy contained in the 3 EMC sections around the beam impact position, in the case of electrons,
- subtracting the noise contribution (90 MeV at the PS and 213 MeV at the SPS) in the case of hadrons,
- subtracting for $E > 10$ GeV/c the momentum spread of the beam which was determined to be about 1% for the collimator settings used during the measurements.

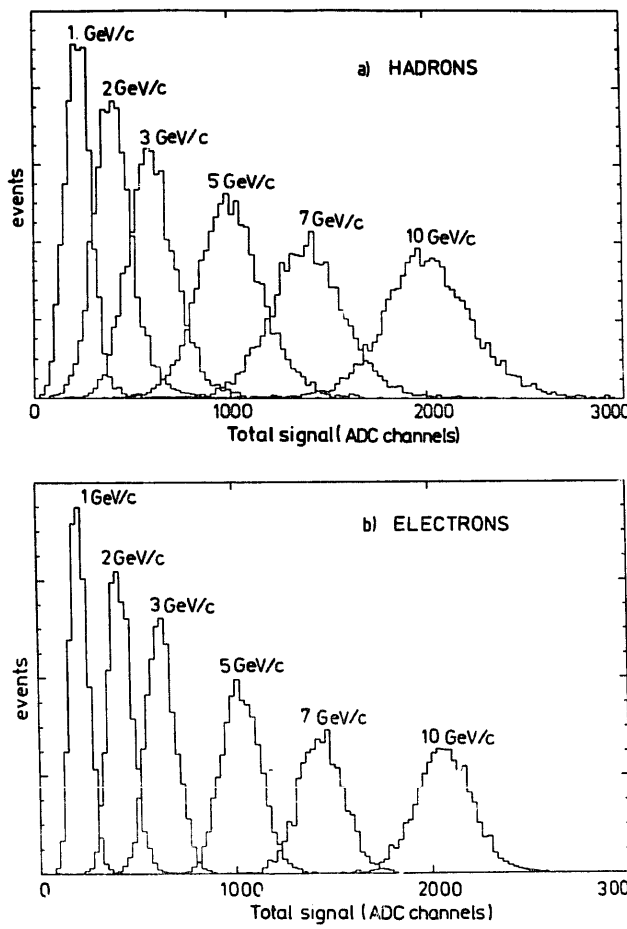

Fig. 25. Pulse height distributions for (a) hadrons and (b) electrons obtained at the PS by summing all calorimeter channels. The distributions are normalized to the same number of events.

* The ZEUS DU calorimeter is surrounded by a backing calorimeter consisting of 75 mm iron slabs sandwiching proportional tubes, to be used as tail-catcher. Experimental tests with a prototype have shown that by adding the energy leaking into the backing calorimeter, no significant degradation in the energy resolution of the uranium calorimeter for hadrons is observed.

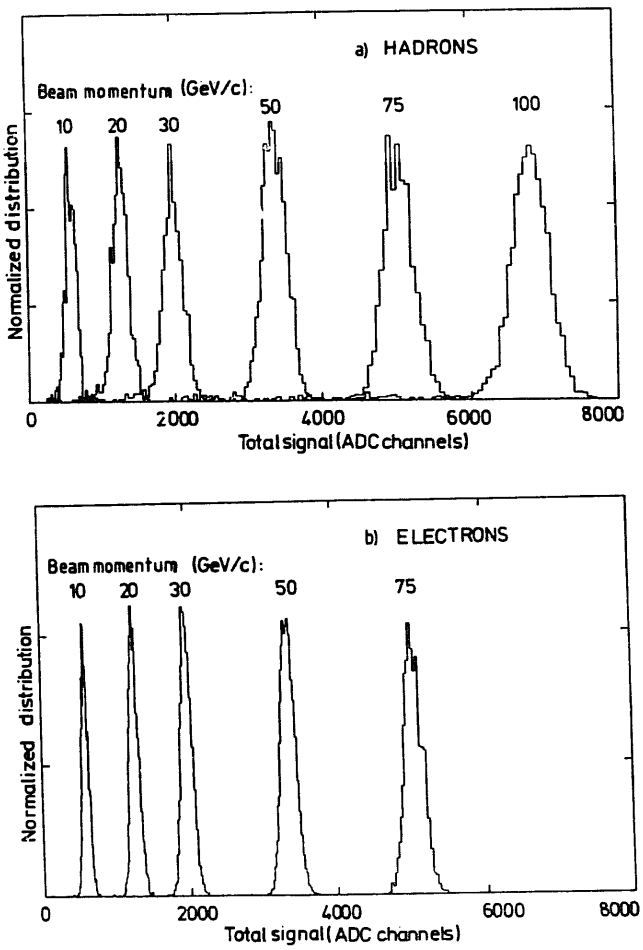

Fig. 26. Pulse height distributions for (a) hadrons and (b) electrons obtained at the SPS by summing all calorimeter channels. The distributions are normalized to the maximum number of events.

The average electron response is reported in table 6 and plotted in fig. 28a. The deviations from linearity are found to be small, at the 1% level. The e/h ratio is reported in table 7 and plotted against beam momentum in fig. 28b. The measured value is rather constant and very close to 1, especially for $E > 10$ GeV/c. For $E < 10$ GeV/c we have to take into account that only 3 modules were read out and we estimate the reduction in hadronic energy to be about 1%. A significant decrease in e/h is observed for a beam momentum of 1 GeV/c. This decrease is expected since e/h should approach the e/mip value of about 0.6 for very low particle momenta. The corrected energy resolution for electrons and hadrons is plotted against beam momentum in fig. 28c. For $E > 2$ GeV/c, the energy resolution for hadrons is on the average $35\%/\sqrt{E}$, in agreement with previous test measurements [2]. The energy resolution for electrons is on the average $18\%/\sqrt{E}$. As discussed before the photostatistics contribution to this value is $10\%/\sqrt{E}$, sampling fluctuations alone being $15\%/\sqrt{E}$ in agreement with Monte Carlo calculations [10].

10. Shower containment and e/h

Electromagnetic showers are fully contained in the four EMC sections of one tower (20×20 cm^2 in cross-section), provided that the beam is incident at the centre of the tower. For hadronic showers, on the contrary, the energy is spread over all calorimeter sections of several towers. The fraction of energy deposited on each calorimeter section (EMC, HAC1 and HAC2) is reported in table 8 and plotted in fig. 29a as a function of the beam momentum. We observe a logarithmic rise with the beam momentum of the energy deposited in the HAC sections. Around $E = 3$ GeV/c, the energy is equally distributed between EMC and HAC sections, whereas for $E = 100$ GeV/c the EMC sections contain only about 20% of the total energy. At the highest beam momentum of 100 GeV/c, the HAC2 sections contain 17% of the total energy. This energy, however, fluctuates considerably from shower to shower.

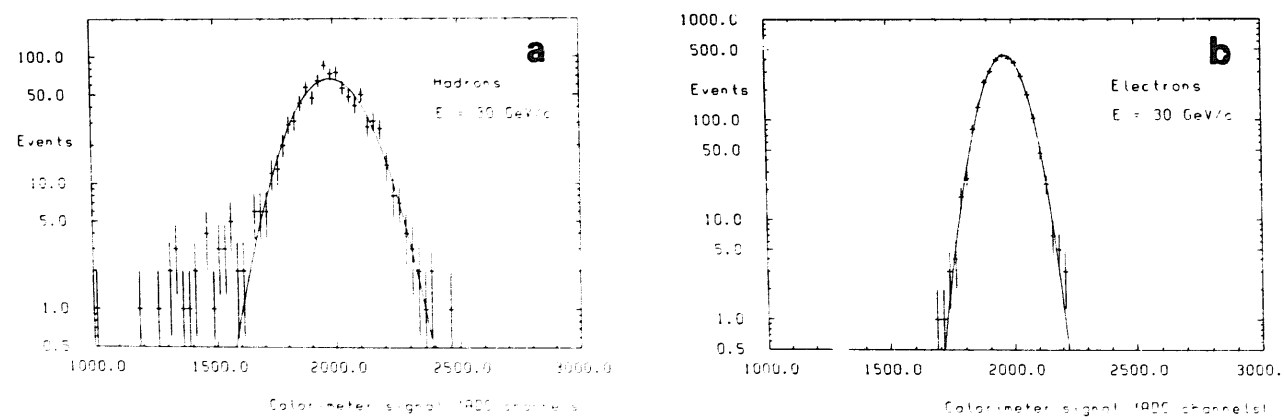

Fig. 27. Pulse height distributions for (a) hadrons and (b) electrons at 30 GeV/c. The number of events is in logarithmic scale and the Gaussian fits are shown.

Table 6
Linearity and energy resolution for electrons. At 100 GeV/c the signal was in saturation. The corrected energy resolution has been obtained by summing up only 3 EMC sections and subtracting 1% beam momentum spread

E [GeV/c]	$\langle E_e\rangle/E$ [ADC ch./GeV]	δ Linearity	$\sigma_e/\langle E_e\rangle\cdot\sqrt{E}$ [%] Uncorrected	$\sigma_e/\langle E_e\rangle\cdot\sqrt{E}$ [%] Corrected
1	210.4±0.8	1.011±0.004	21.7±0.3	18.5±0.3
2	210.5±0.5	1.013±0.003	19.8±0.3	18.1±0.3
3	209.6±0.3	1.009±0.002	19.5±0.3	18.9±0.3
5	205.5±0.3	0.989±0.002	19.3±0.3	18.6±0.3
7	204.3±0.3	0.984±0.001	19.3±0.3	19.2±0.3
10	205.9±0.2	0.991±0.001	18.7±0.3	18.7±0.3
10	64.9±0.1	0.989±0.001	20.9±0.3	18.7±0.3
20	65.0±0.1	0.991±0.001	19.4±0.3	17.8±0.3
30	65.6±0.1	1.000±0.001	19.1±0.3	17.5±0.3
50	66.0±0.1	1.006±0.001	20.0±0.3	18.3±0.3
75	66.4±0.1	1.012±0.001	19.8±0.3	17.6±0.3
100	–	–	–	–

As explained in the previous section, only showers with less than 10% of the energy in the HAC2 were selected for the e/h measurement.

Hadronic showers are also spread over many calorimeter towers as shown in fig. 29b. This figure was obtained from a scan with the 30 GeV/c hadron beam incident at the centre of each calorimeter tower. It is possible to obtain in this way the average energy deposited on each tower of a 7×7 towers calorimeter (140×140 cm^2 in cross-section) from the information collected by the 4×4 towers calorimeter. A similar result was obtained for 5 GeV/c hadron showers, thus indicating that the lateral spread is rather energy independent. We observe that the central tower, where the beam is incident, contains 75.5% of the total energy, and the 4×4 towers calorimeter used in the test, 97.2%. The e/h ratio ranges from 1.02 for the 3×3 calorimeter to 0.97 for the 7×7 calorimeter (see table 9).

As a conclusion, the e/h ratio is slightly dependent on the total number of towers summed up to get the total energy. We note, however, that it is always possible to retune e/h by changing the intercalibration parameter α (see section 6.3). Other parameters which might have some influence on e/h are:
- the dead material in front of the calorimeter,
- the angle of incidence of particles entering the calorimeter,

Table 7
e/h ratio and energy resolution for hadrons. The corrected resolution has been obtained by subtracting the noise (90 MeV for $E<10$ GeV/c, 213 MeV for $E>10$ GeV/c) and 1% beam momentum spread. The data for $E<10$ GeV/c have been obtained with only 3 modules.

E [GeV/c]	e/h	$\sigma_h/\langle E_h\rangle\cdot\sqrt{E}$ [%] Uncorrected	$\sigma_h/\langle E_h\rangle\cdot\sqrt{E}$ [%] Corrected
1	0.92±0.01	28.9±0.5	27.5±0.5
2	1.03±0.01	34.0±0.4	33.4±0.4
3	1.03±0.01	34.2±0.3	33.8±0.3
5	1.03±0.01	35.5±0.3	35.3±0.3
7	1.02±0.01	35.7±0.3	35.5±0.3
10	1.01±0.01	35.2±0.3	35.1±0.3
10	1.01±0.01	36.4±0.3	35.1±0.3
20	1.00±0.01	36.2±0.3	35.4±0.3
30	1.00±0.01	35.8±0.3	35.0±0.3
50	1.00±0.01	35.5±0.3	34.6±0.3
75	1.00±0.01	35.6±0.3	34.6±0.3
100	1.00±0.01	36.7±0.3	35.0±0.3

Table 8
Fraction of energy deposited by hadron showers in the different calorimeter sections as a function of the beam momentum

E [GeV/c]	E_{EMC} [%]	E_{HAC1} [%]	E_{HAC2} [%]
1	56.0	43.2	0.9
2	50.4	46.4	3.2
3	46.5	50.1	3.4
5	41.5	53.9	4.6
7	37.9	56.4	5.7
10	32.0	61.0	7.0
20	27.8	61.8	10.3
30	25.8	61.2	13.0
50	23.8	61.7	14.5
75	21.5	62.1	16.5
100	21.1	62.0	16.9

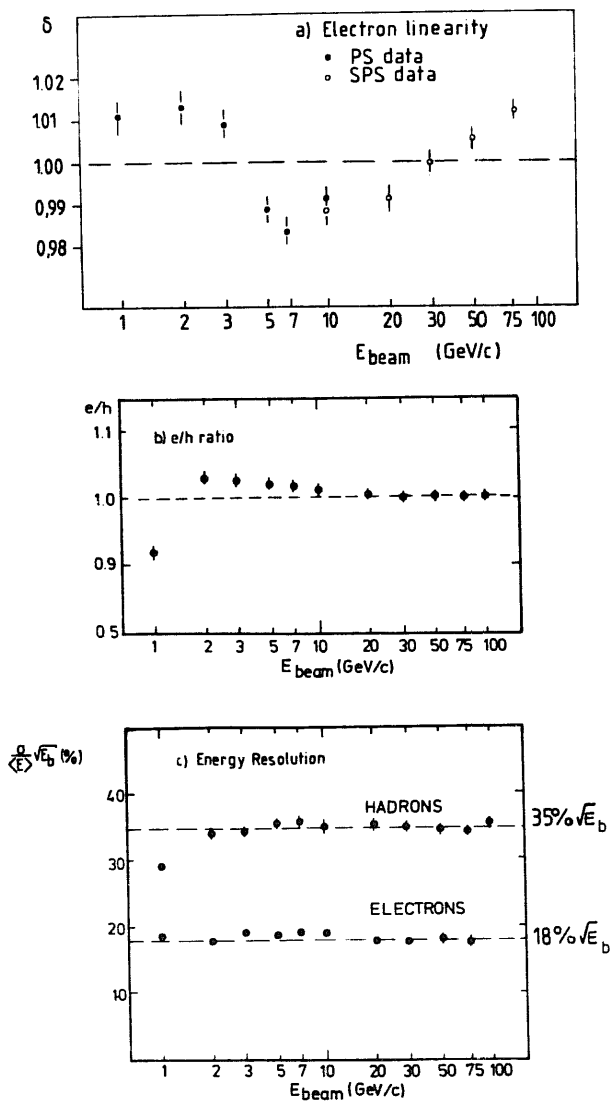

Fig. 28. (a) Electron linearity. The parameter $\delta = \langle E_e \rangle / E_{beam}$ normalized to its average value is plotted versus beam momentum. The normalizations for PS and SPS data are independent. (b) e/h ratio versus beam momentum. The data below 10 GeV/c were obtained with only 3 modules. All calorimeter channels have been added to obtain both e and h. (c) Energy resolution versus beam momentum for electrons (only 3 EMC sections summed up) and hadrons (all channels summed up).

- the effective gate used to integrate the PM pulses.

A discussion of the influence of all these effects on e/h is beyond the scope of this article.

11. Overall energy resolution of the FCAL

Taking into account the results on calibration, uniformity and noise reported in the previous sections, the expected energy resolution of the FCAL is of the form:

$$\frac{\sigma_E}{E} = \frac{\sigma_{noise}}{E} \oplus \frac{a}{\sqrt{E}} \oplus b \quad (E \text{ in GeV}),$$

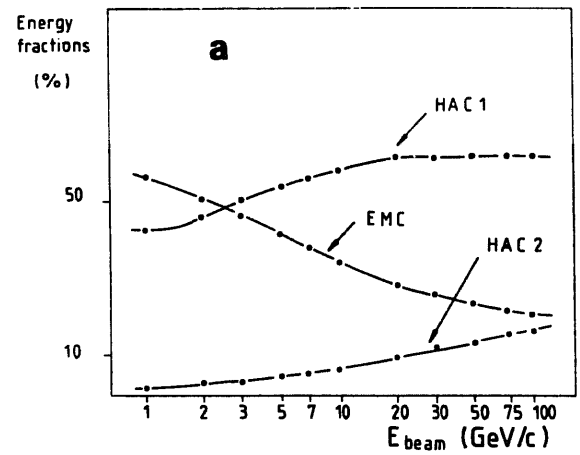

b Lateral spread of 30 GeV/c hadron showers

0.01	0.02	0.07	0.04	0.07	0.02	0.01
0.02	0.09	0.25	0.30	0.25	0.09	0.02
0.07	0.25	1.3	3.7	1.3	0.25	0.07
0.04	0.30	3.7	75.5	3.7	0.30	0.04
0.07	0.25	1.3	3.7	1.3	0.25	0.07
0.02	0.09	0.25	0.30	0.25	0.09	0.02
0.01	0.02	0.07	0.04	0.07	0.02	0.01

Total sum = 100

Fig. 29. (a) Fraction of energy deposited by hadron showers in the different calorimeter sections as a function of the beam momentum. (b) Lateral spread of 30 GeV/c hadron showers. Each cell represents a 20×20 cm^2 calorimeter tower. The beam is incident in the middle of the central tower and the sum of all cells is normalized to 100.

where the first term is the noise contribution, the second term the contribution of intrinsic, sampling and photoelectron fluctuations, and the third term the contribution of calibration errors and nonuniformities. The magnitude of these 3 terms is discussed below.

According to the results of section 9, the value of a should be 18% for electrons and 35% for hadrons. A

Table 9
Hadron shower containment and e/h as a function of the calorimeter transverse size for 30 GeV/c particles. Each tower is 20×20 cm^2 in cross-section

Transverse size (towers)	Shower Containment	e/h
1×1	75.5%	1.29
3×3	95.5%	1.02
4×4	97.2%	1.00
5×5	99.1%	0.98
7×7	100.0%	0.97

small increase in a can be expected in the case of electrons entering the calorimeter at large angles of incidence.

In the final electronics it is foreseen to read out every PM by a high and a low gain channel. Therefore the reduction in PM gain necessary to take data at high momenta during the test will be avoided. If it is possible to reduce the coherent noise between individual channels to a negligible level as for the prototype test, we can assume a uranium dominated noise of 25 MeV per tower. In this case $\sigma_{noise} = 2.5\% \times \sqrt{N_t}$ where N_t is the number of towers summed up to get the total signal. Typically $N_t \sim 1$ for isolated electrons * and $N_t \sim 16$ for isolated hadrons. The maximum value of σ_{noise} is 0.5 GeV, when all 460 towers of the FCAL are summed up. This value is still small compared to typical total energies deposited in the FCAL. We should point out again that the final electronics is significantly different from the one used during the test and some of the results presented here, in particular the noise value, depend of course on it.

The parameter b is due to calibration errors and nonuniformities. We can assume the following contributions:

- accuracy of the UNO signal to detect PM gain variations: 1%,
- stability of the UNO signal, for measurements performed, for example, every 8 hours: 1%,
- average nonuniformity contributions from particles hitting the calorimeter at the boundaries between modules: 1%,
- residual nonunformities from particles hitting at the boundaries between EMC sections or close to a spacer: 1%.

Adding all those effects we obtain a value for b of about 2%. We note that the most important contributions to b come from the EMC sections. The expected value of b for hadron showers is therefore possibly smaller.

All these results on energy resolution assume no dead material in front of the calorimeter. According to the design of the ZEUS detector [1], the dead material traversed by particles entering the calorimeter is typically $1X_0$ and some degradation of the energy resolution is therefore expected, especially at low energies. A study of this effect will not be included here.

12. Position resolution

The position resolution of the calorimeter has been investigated for isolated electrons and hadrons, under normal incidence.

* The noise of the EMC sections is only 15 MeV per tower. However the energy of an isolated electron might be spread over several EMC towers.

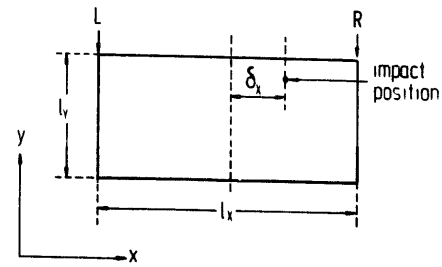

Fig. 30. Coordinate system used to reconstruct the centre of gravity of the deposited energy in one calorimeter section.

The coordinate system used for position reconstruction is shown in fig. 30. Assuming an exponential light attenuation along the scintillator in the x direction, the distance from the centre of gravity of the deposited energy to the middle of a section can be calculated according to

$$\delta x = \frac{\lambda}{2} \ln \frac{E_R}{E_L},$$

where E_R and E_L are the right and left energy depositions and λ the scintillator attenuation length. Fig. 31 shows δx as a function of E_R/E_L for 5 GeV/c electrons incident along the x axis at the middle of the strip. We observe that δx is a logarithmic function of E_R/E_L with $\lambda \approx 54$ cm except close to the section boundary due to the WLS effect studied in section 7 (the data presented here were taken with no lead foil between the modules and an ad hoc correction has been introduced in this region).

We have used the following algorithms to reconstruct the position of incident particles:

$$x = \sum_i w_i x_i \quad \text{and} \quad y = \sum_i w_i y_i,$$

with $x_i = (x_0)_i + \delta x_i$, $y_i = (y_0)_i$ and $w_i = E_i/E$. The quantities $(x_0)_i$, $(y_0)_i$ and E_i are the central coordinates and the energy deposited in each calorimeter section; E is the total calorimeter energy and δx_i the position correction mentioned previously. The sums run over all calorimeter sections.

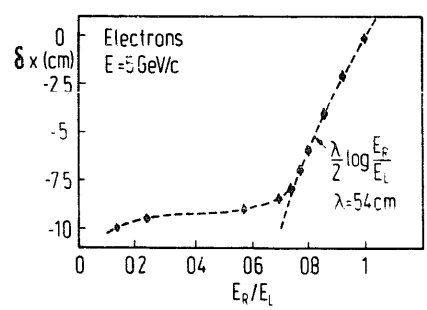

Fig. 31. Distance δx between the centre of gravity of the deposited energy and the middle of an EMC section, as a function of the ratio E_R/E_L of right and left readout energies.

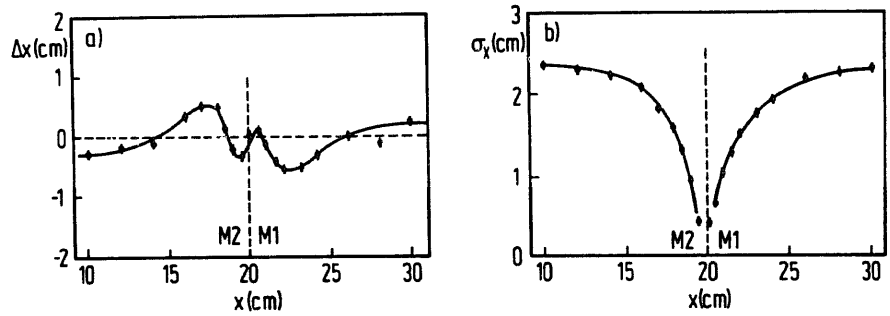

Fig. 32. Horizontal position reconstruction for 5 GeV/c electrons under normal incidence showing (a) the shift in the average reconstructed position and (b) the position resolution.

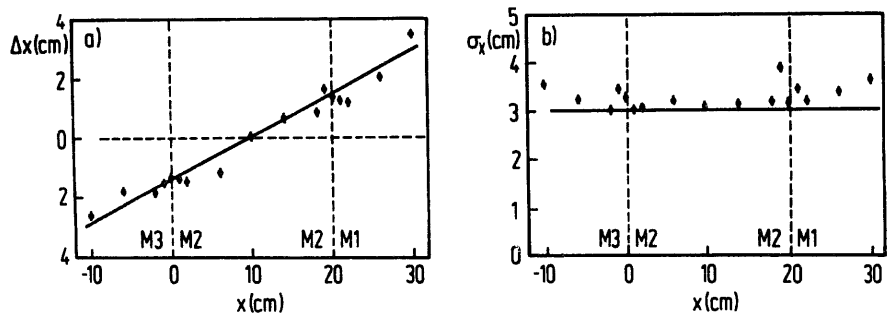

Fig. 33. Horizontal position reconstruction for 5 GeV/c hadrons under normal incidence showing (a) the shift in the average reconstructed position and (b) the position resolution.

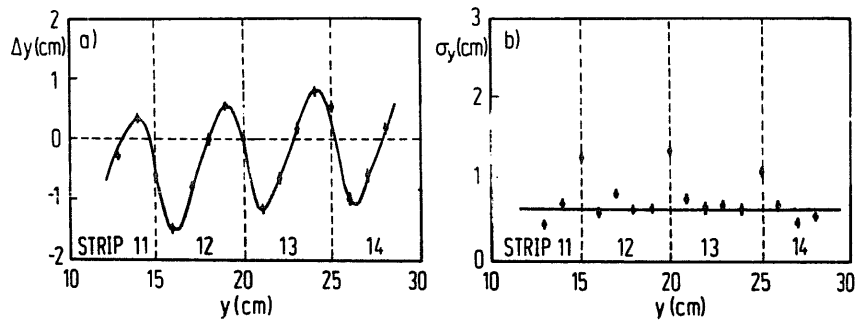

Fig. 34. Vertical position reconstruction for 5 GeV/c electrons under normal incidence showing (a) the shift in the average reconstructed position and (b) the position resolution.

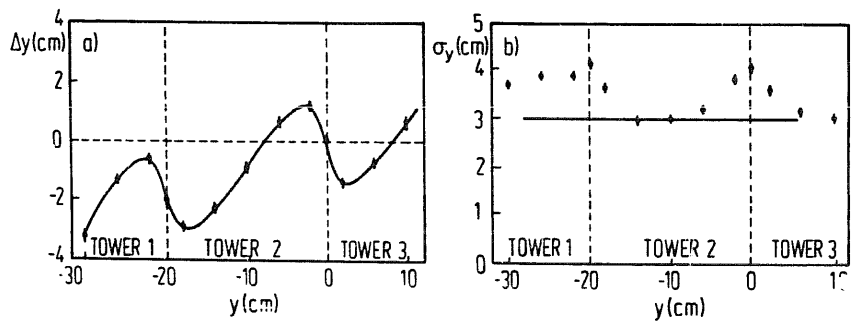

Fig. 35. Vertical position reconstruction for 5 GeV/c hadrons under normal incidence showing (a) the shift in the average reconstructed position and (b) the position resolution.

In addition to the position resolutions σ_x and σ_y, we have to consider the shifts Δx and Δy in the average positions, introduced by the reconstruction algorithm. Fig. 32a and 32b display Δx and σ_x for a 5 GeV/c electron horizontal scan between modules in 1 and 2. The result of a similar scan with 5 GeV/c hadrons covering a larger region in x is displayed in figs. 33a and 33b. We observe some shifts in the electron position reconstruction close to the module boundaries. In the hadron case the shift can be explained entirely by the energy leakage to the sides. The expected position resolution at the center of a section is

$$\sigma_x = \lambda\sigma_d \quad \text{with} \quad \sigma_d = \frac{\sigma(E_R - E_L)}{\langle E_R + E_L\rangle}.$$

For electrons σ_d is simply the photostatistics, $10\%/\sqrt{E}$, and for hadrons $\sigma_d \approx 12\%/\sqrt{E}$, therefore we expect

$$\sigma_x \approx \frac{5.4}{\sqrt{E}} \text{ cm (electrons)}$$

and

$$\sigma_x \approx \frac{6.5}{\sqrt{E}} \text{ cm (hadrons)}.$$

These values are in agreement with the measured values for $E = 5$ GeV/c particles. The calorimeter response to electrons is very sensitive to the impact position close to module boundaries, therefore the position resolution is also improved in this region (see fig. 32b). This effect is however smeared as the angle of incidence increases. These results are not affected by the horizontal beam width of $\sigma_x(b) \approx 0.2$ cm.

The shifts Δy in the vertical position reconstruction are more important, since all the energy deposited in a section is assigned to the center of the section. Figs. 34 and 35 display the results obtained for 5 GeV/c electrons and hadrons, respectively. The shift Δy is an oscillation of 1 cm amplitude for both electrons and hadrons (in the hadron case there is an additional shift due to leakage). The shift Δy vanishes at the center and boundaries of EMC or HAC sections for electrons or hadrons, respectively. The position resolutions are $\sigma_y \approx$ 0.6 cm (electrons) and 3.0 cm (hadrons). The beam width in the vertical direction, $\sigma_y(b) \approx 1$ cm has in this case a non-negligible influence on the result close to section boundaries. Assuming a scaling of σ_y with $\sqrt{E}$, we find

$$\sigma_y \approx \frac{1.4}{\sqrt{E}} \text{ cm (electrons)}$$

and

$$\sigma_y \approx \frac{6.7}{\sqrt{E}} \text{ cm (hadrons)}.$$

If the impact position of the particle is random, the shift Δy introduces a constant term in the vertical position resolution:

$$\sigma_0 = \left[\frac{1}{l_y}\int_0^{l_y}(\Delta y)^2 dy\right]^{1/2} \approx 0.7 \text{ cm}$$

both for electrons and hadrons, l_y being the vertical length of one calorimeter section. The position resolutions under normal incidence are summarized in table 10. The vertical position resolution can be improved by using more sophisticated algorithms (see for example [11]).

Table 10
Horizontal and vertical position resolutions for isolated electrons and hadrons under normal incidence; E is the shower energy in GeV

	σ_x [cm]	σ_y [cm]
Electrons	$5.4/\sqrt{E}$	$1.4/\sqrt{E} \oplus 0.7$
Hadrons	$6.5/\sqrt{E}$	$6.7/\sqrt{E} \oplus 0.7$

13. Summary

Four prototype uranium–scintillator sandwich calorimeter modules following the design of the final ZEUS FCAL modules have been constructed and tested with electrons, hadrons and muons in the momentum range of 1 to 100 GeV/c. The main results of the test are:

(1) The uranium radioactivity signal (UNO signal) can be used to detect PM gain variations with an accuracy of $\pm 1\%$. Typical PM gain variations measured with the prototype modules were 1% after 8 hours of running. By balancing the UNO signal in sections which are geometrically identical, an intercalibration of the PM gains can be obtained. This intercalibration agrees within 2 to 3% with an intercalibration obtained with beam particles.

(2) An important source of nonuniformities in the electron response has been localized at the boundaries between adjacent modules. These nonuniformities, which can be as big as 60% for normal beam incidence, are suppressed by inserting a 2 mm thick lead foil between the modules. Taking into account that particles hit the FCAL module boundaries under a minimum angle of 40 mrad, the expected overall effect of residual nonuniformities in the electron response and resolution are below 1%. No significant nonuniformities have been observed for hadron showers.

(3) An electron linearity within $\pm 1\%$ and a ratio e/h close to 1 have been measured over the whole momentum range except for the lowest momenta (below 2 GeV/c) where some increase in the hadron response

has been observed. The expected energy resolution for the FCAL is

$$\frac{\sigma_E}{E} = \frac{\sigma_{\text{noise}}}{E} \oplus \frac{a}{\sqrt{E}} \oplus b \quad (E \text{ in GeV}),$$

where $\sigma_{\text{noise}} = 25$ MeV/tower assuming a total noise dominated by the uranium noise, a is equal to 18% for electrons and 35% for hadrons, and $b \sim 2\%$ taking into account calibration errors and nonuniformities.

(4) The position resolution obtained with the help of simple algorithms for isolated particles after normal incidence is:

- for electrons, $\sigma_x = (5.4/\sqrt{E})$ cm and $\sigma_y = (1.4/\sqrt{E} \oplus 0.7)$ cm,
- for hadrons, $\sigma_x = (6.5/\sqrt{E})$ cm and $\sigma_y = (6.7/\sqrt{E} \oplus 0.7)$ cm,

x and y being the horizontal and vertical directions respectively.

Acknowledgements

The test has been possible thanks to the enthusiastic support of the technical staff from the collaborating institutes for the construction, transport, frequent improvements and modifications of the modules as well as the help in setting up the experiment. We want to thank in particular R. Abarca, R. Blankers, A. Cerrato, P. Greenwood, J. Hauschildt, J. Homma, P. Hunck, S. Iaccino, F. Jarvis, A. Kiang, K. Loeffler, D. Mosscrop, H. Sabath and K. Westphal. We are also grateful for the hospitality and support of CERN, related in particular to the transport of the uranium modules. We also want to thank the CERN Radiation Safety Service and in particular G. Roubaud, and K. Bätzner, P. Grafström and D. Plane for their help in setting up the beam. Finally we want to thank all our colleagues from the ZEUS collaboration who helped to perform the test and in particular E. Hilger, E. Lohmann, F. Sciulli and G. Wolf for support and helpful discussions.

References

[1] ZEUS, a detector for HERA, Letter of Intent, DESY (June 1985).
The ZEUS detector, Technical Proposal, DESY (March 1986);
The ZEUS detector, Status Report 1987, DESY (September 1987);
The ZEUS detector, Status Report 1989, DESY (March 1989).

[2] T. Akesson et al., Nucl. Instr. and Meth. A241 (1985) 17;
B. Anders et al., DESY 86-105 (Sep. 86);
T. Akesson et al., Nucl. Instr. and Meth. A262 (1987) 243;
G. d'Agostini et al., Nucl. Instr. and Meth. A274 (1989) 134.

[3] H. Brückmann, Hadron calorimetry – a puzzle of physics, Proc. Workshop on Compensated Calorimetry, Pasadena (1985) CALT-68-1305.

[4] J. Brau and T. Gabriel, Nucl. Instr. and Meth. A238 (1985) 489;
H. Brückmann et al., DESY 86-155 (1986);
R. Wigmans, Nucl. Instr. and Meth. A259 (1987) 389.

[5] Product of Kyowa-Gas, Japan;
T. Kamon et al., Nucl. Instr. and Meth. 213 (1983) 261.

[6] U. Holm and K. Wick, IEEE Trans. Nucl. Sci. NS-36 (1989) 579.

[7] Quality Q173D from Du Pont.

[8] Product of Kyowa-Gas, Japan.

[9] W. Buttler et al., Nucl. Instr. and Meth. A277 (1989) 217;
B. Sippach et al., Development of the front end electronic for the ZEUS calorimeter, Contribution of the IEEE Symp., Orlando, Florida (1988).

[10] W.R. Nelson, H. Hirayama and D.O. Rogers, SLAC-265 (1985).

[11] G.A. Akopdjanov et al., Nucl. Instr. and Meth. 140 (1977) 441.